Modelling TCE Contaminant Transport in Fractured Bedrock and Evaluating Bedrock Vapour Extraction using CompFlow BioF at CTL-III, Santa Susana Field Laboratory

by

Khatoon Motakefghomi

A thesis

presented to the University of Waterloo

in fulfillment of the

thesis requirement for the degree of

Master of Science

in

Earth Sciences (Water)

Waterloo, Ontario, Canada, 2026

© Khatoon Motakefghomi 2026

Author's Declaration

I hereby declare that I am the sole author of this thesis. This is a true copy of the thesis, including any required final revisions, as accepted by my examiners.

I understand that my thesis may be made electronically available to the public.

Abstract

Numerical simulation of contaminant transport and remediation in fractured bedrock remains a significant challenge due to strong geological heterogeneity, multiphase flow behavior, and uncertainty in subsurface properties. Chlorinated solvents such as trichloroethylene (TCE) are particularly problematic in these environments, as fracture-controlled flow can accelerate migration and mass stored in the matrix between the fractures complicates remediation efforts.

The primary aim of this research is to simulate a real bedrock vapour extraction (BVE) pilot test. TCE transport and vapour-phase remediation in fractured bedrock at the Santa Susana Field Laboratory (SSFL), California, are modeled using the multiphase, multicomponent numerical simulator CompFlow BioF. The modeling framework incorporates: discrete fracture representations; capillary pressure and relative permeability relationships for the mobile aqueous, gas and non-aqueous phases; and, equilibrium phase partitioning between the aqueous, gas and non-aqueous phases to capture key processes governing contaminant behavior in the vadose zone. Site-specific geological conditions and operational parameters from the field-scale BVE test were used to configure the numerical domain, enabling simulation of both contaminant phase and mass distributions evolution and active remediation scenarios.

Simulation results were compared with field observations to evaluate the model's ability to reproduce observed contaminant distributions and subsurface moisture conditions. The comparison demonstrates that the model captures lateral and vertical variability in TCE occurrence and water content across multiple monitoring locations, as well as long-term changes in contaminant phase distribution. These findings provide confidence in the model's representation of fracture–matrix interactions and multiphase flow and transport processes in unsaturated fractured bedrock.

Overall, it demonstrates the value of integrating numerical modeling with field-scale pilot testing, both informed at the process scale to improve conceptual understanding of fractured bedrock systems and to support the design and evaluation of remediation technology effectiveness from a time and cost perspective for chlorinated solvent contamination.

Acknowledgements

First and foremost, I would like to express my sincere appreciation to my supervisors, Dr. Andre Unger and Dr. Ken Walton, for their guidance, mentorship, and steadfast support throughout this research. Their dedication, expertise, and thoughtful advice were fundamental to the successful completion of this work.

I also extend my gratitude to my thesis committee members, Dr. Beth Parker and Dr. Andrea Brookfield, for their insightful feedback, scholarly contributions, and ongoing support. Financial support for this research was generously provided by The Boeing Company and through an Industrial Research Chair grant from the Natural Sciences and Engineering Research Council of Canada, held by Dr. Parker. This grant also supported the collection of novel field data used to inform this modeling exercise.

Finally, but not at all in the least, I am grateful to my parents for nurturing my independence and for their constant encouragement and sacrifices as I pursued my future, even when it meant building a life far from them. I equally owe a profound debt of gratitude to my husband, Mohammad, whose encouragement motivated me to pursue and apply for my master's degree.

Dedication

To my beloved parents, **Parvin** and **Mohammad**.

Table of Contents

Author's Declaration ii
Abstract iii
Acknowledgements iv
Dedication v
List of Figures vii
List of Tables x
List of Abbreviations xi
List of Symbols xii
Chapter 1 Introduction 1
1.1 Background and Motivation 1
1.2 Site Characterization 3
1.3 Objectives and Scope 5
1.4 Thesis Organization 6
Chapter 2 Literature Review 7
2.1 Site-Specific Hydrogeology of the Santa Susana Field Laboratory (SSFL) 7
2.2 Theoretical Framework of DNAPL in Fractured Media 7
2.3 Challenges in Applying Vapour Extraction 7
2.4 Description of the CTL-III and BVE Pilot Test Areas 8
Chapter 3 Methodology 10
3.1 Conceptual Site Model 11
3.2 Subsurface Material Properties at CTL-III 12
3.3 Numerical Model 15
3.3.1 Computational Domain and Boundary Conditions 15
3.3.2 Governing Equations and Multiphase Flow Properties 19
3.4 Postprocessing of Numerical Model Outputs for Comparison to Field Data 21
3.4.1 Water Content 21
3.4.2 TCE Concentration 21
Chapter 4 Results 23
4.1 Origin and Transport of TCE Contamination 23
4.1.1 Comparison of Simulated to Measured Water Distribution 23
4.1.2 Comparison of Simulated to Measured TCE Distribution 26
4.2 BVE Pilot Study 35
4.2.1 Comparison of Simulated to Measured Vacuum Response 35
4.2.2 Simulated TCE Vapour Response 40
4.2.3 Simulated Water Infiltration Response 42
4.3 Impact of BVE on Vadose Zone TCE Mass Removal and Groundwater Flux Reduction 44
Chapter 5 Conclusions 48
References 50

List of Figures

Figure 1 : Aerial view of the CTL-III and BVE Pilot Test area, including locations of cored holes/monitoring wells, and BVE extraction well. Inset: Location of the Santa Susana Field Lab in the state of California, USA. 5

Figure 2 : Workflow for TCE modelling and BVE evaluation at CTL-III. 10

Figure 3 : Schematic of the subsurface lithologic of layers in the model domain (black outline) and applied boundary conditions, including surface flux, $R_{ambient}$ and $R_{pond}(t)$, NAPL loading, $Q_{NAPL}(t)$, gas exchange (gray arrows), water table position and hydraulic gradient (blue arrows). The left panel shows the boundary conditions that were considered during epoch 1, 2 and 3 (legacy contaminant transport modelling) and the right panel shows boundary conditions that were considered during epoch 4 and 5 (BVE remediation modelling). 12

Figure 4 : BV-1, BV-3 and C-33 rock core moisture content and NMR (Figure 6,9 and 17 of Manna et al., 2025) 13

Figure 5 : a) Discretization of the PM. b) DFN used to inform numerical discretization. The 2-D x–z section displays fractures colour-mapped by aperture length, with warmer tones indicating wider aperture and higher transmissivity. c) Multi-layered lithologic units interpreted from Gamma-Ray data. 17

Figure 6 : Frequency distribution of fracture aperture sizes in the simulation's discrete fracture network (Left); Vertical Distribution and Cumulative Count of Fractures per Meter Depth (P_{10}) from the profile at x=60 m (right). 18

Figure 7 : Capillary pressure and relative permeability relationships for the Chatsworth formation matrix as well as for a 100-micron fracture. 21

Figure 8 : Simulated water saturation distribution across the numerical domain. The 2-D cross-section (left) illustrates the contrast between the porous matrix and the discrete fracture network and spatial variability in saturation in the vadose zone. The three vertical profile plots (right) compare the saturation of the Porous Medium against the Fracture network as a function of depth. 25

Figure 9 : Integrated comparison of CFBioF-simulated water content profiles with 2023 field measurements (Jacobs, 2025) at three horizontal positions. 26

Figure 10 : Numerical simulation of TCE saturation index (SI) evolution for the years 1960, 1970, and 1971, showing DNAPL and its subsequent disappearance driven by–dissolution processes. Note: the zoomed insets show DNAPL presence at 1960 (mobile, dark red) through 1970 (residual, plum), and solute only in 1971 (magenta). The perched water table at the alluvium-bedrock interface is outlined in blue. 27

Figure 11 : Spatial visualizations of the simulated Total Equivalent TCE (all phases) mass fraction within the bulk wet rock (TCE Content) at three pre-BVE time snapshots, superimposed on the intrinsic vertical permeability field of the rock matrix (kzz): 1960, marking the end of TCE DNAPL injection in the pond; 1972, marking the cessation of enhanced pond infiltration; and 2023, immediately prior to BVE implementation. Vertical markers on the 2023 panel denote the locations of the vertical profiles corresponding to BV-3, BV-1, and C-33. 30

Figure 12 : Simulation results expressed as equivalent, all-phases TCE mass fraction in rock, compared with core-derived TCE mass fraction measurements at three core locations (BV-3, BV-1, RD-46b/C-33, replotted from (Jacobs, 2025, Appendix A) and corresponding positions in the simulation domain. Lower and Upper bound mass fraction estimates are computed by applying site-observed porosity and bulk density variability point-wise to the simulated aqueous TCE concentrations. 32

Figure 13 : Spatial distribution of total equivalent TCE within the rock matrix (colour fill) as interpolated from rock core measurements (dots in well traces) into a 3-D geologic block model (Weaver, 2026, personal communication). 'Variably Saturated' describes the changing water table elevation during the Pilot Test, from the drilling of holes to the monitoring of the BVE operations, rather than rock matrix pore water conditions. The red dashed box indicates the approximate extent of mass summation appearing in other figures, for spatial reference. 34

Figure 14 : a) Measured gas pressure distribution within the fractured bedrock domain during active Bedrock Vapour Extraction. (Appendix A – MG360 – SSFL CTL-III BVE Pilot Test Report 2025). b) Simulated gas-phase vacuum pressures (iso-lines) distribution within the fractured bedrock domain during active BVE (reported as a fractional year). The red dashed box in both panels indicates the approximate spatial extent of mass summation from the 3D interpolated geologic block model. 37

Figure 15 : Simulated profiles of gas phase pressure (P_g) and velocity magnitude ($|v_g|$) for locations BV-3, BV-1, and C-33 at times before BVE (2023.0), near the end of BVE (2024.1) and immediately following BVE (2024.2) 39

Figure 16 : Vertical water saturation profiles before, during (near end) and after BVE (+10 months) in the simulated borehole locations BV-3, BV-1, and C-33. 40

Figure 17 : Vertical TCE concentrations in the gas phase before, during (near end) and at near and future times after BVE in the analogous simulated borehole locations BV-3, BV-1, and C-33. 42

Figure 18 : Simulation results showing porous medium versus fracture aqueous phase discharge (as solid lines) and discharge proportion (as dashed lines) over horizontal planes at various elevations in the vadose zone (elevations as indicated). 43

Figure 19 : Simulated evolution of TCE mass and TCE rates in the 2-D simulation domain. (a) Long-term view of resident mass, cumulative losses due to discharge to the water table and decay from 1960 to 2060. (b) Short-term view of mass from 2023 to 2025, focused on the time surrounding the BVE operational period. (c) Long-term mass-loss rates due to BVE, discharge to the water table and decay. (d) Short-term view of mass-loss rates surrounding the BVE operational period. 45

Figure 20 : Cumulative TCE mass removed during BVE operations, calculated using interval-averaged influent concentrations and flow rates. Short-term variability in system flow and temporal declines in influent concentration is not reflected in this estimate. Reprinted Figure 11-8 from (Jacobs, 2025). 46

List of Tables

Table 1 : Summary of hydrogeological and geochemical model input parameters for contaminant transport simulation. 14

Table 2 : Total equivalent TCE mass from a 40 m-wide, unit-thickness cut-out from the 3-D geologic block model (Weaver, 2026, personal communication) versus mass in 40 m-wide cutout of the 120 m-wide 2-D simulation. 35

List of Abbreviations

BVE	Bedrock Vapour Extraction
CFBioF	CompFlow Bio with Fractures
CTL-III	Component Test Laboratory III
CVFD	Control Volume Finite Difference
CVOC	Chlorinated Volatile Organic Compounds
DFM	Discrete Fracture-Matrix
DFN	Discrete Fracture Network
DNAPL	Dense Non-Aqueous Phase Liquid
NMR	Nuclear Magnetic Resonance
SSFL	Santa Susana Field Laboratory
TCE	Trichloroethylene
VOC	Volatile Organic Compounds

List of Symbols

d	Depth [m]
δ_{IJ}	Kronecker delta function at matrix indices *I* and *J*
g	Gravitational acceleration constant [m/s^2]
ϕ	Porosity [-]
$\mathbb{K}$	Intrinsic permeability tensor [m^2]
K_d	Sorption coefficient [m^3/kg]
k_{rl}	Relative permeability of phase l [-]
M_l	Molar density of phase l [mol/m^3]
μ_l	Coefficient of dynamic viscosity of phase l [kg m^{-1} s^{-1}]
P_l	Fluid pressure of phase l [kg m^{-1} s^{-2}]
Q_p	Source/Sink term for species p [mol m^{-3} d^{-1}]
ρ_l	Mass density of phase l [kg/m^3]
ρ_b	Bulk density of the porous medium [kg/m^3]
S_l	Saturation of phase l [-]
t	Time [d]
X_{pl}	Mole fraction of species p in phase l [-]
S_w	Water saturation (–)
ρ_w	Density of water [kg/m^3]
$C_{TCE,q}$	Concentration of TCE in an aqueous phase [g/L^3]
$X_{TCE,q}$	The mole fraction of TCE within the aqueous phase [mol/mol]
$\rho_{M,water,q}$	The molar density of water in the aqueous phase [mol/L^3]
M_{TCE}	The molar mass of TCE [g/mol]
R_{matrix}	Rock matrix retardation factor representing linear, instantaneous sorption (-)

Chapter 1
Introduction

1.1 Background and Motivation

Groundwater contamination by chlorinated solvents remains a persistent environmental problem at industrial and military sites worldwide. Among these compounds, trichloroethylene (TCE) has been extensively used as a degreasing and cleaning agent in aerospace, manufacturing, and defence-related activities throughout the twentieth century (EPA, 2011; Pankow & Cherry, 1996). Due to its widespread historical use, improper handling, and disposal practices, TCE is now one of the most detected contaminants in soil and groundwater systems. Its toxicity, persistence, and classification as a human carcinogen have made TCE contamination a major concern for regulators, site managers, and affected communities.

The environmental behaviour of TCE is strongly controlled by subsurface geological conditions. In the vadose (unsaturated) zone, where both air- and water-filled pores coexist, TCE migration as a dense, non-aqueous phase liquid (DNAPL) is governed by multiphase flow processes, including capillary pressure effects, relative permeability, and phase mass transfer between NAPL, aqueous, and gas phases, as well as sorption to the solid matrix. These processes control the redistribution and downward migration of NAPL toward the water table. Once in the saturated zone, unconsolidated sediments typically exhibit porous media flow in which contaminant transport is governed by relatively well-understood advection–dispersion processes. In contrast, fractured bedrock environments present a much greater challenge for contaminant characterization, prediction, and remediation (Bear et al., 1993 ; Freeze & Cherry, 1979). In these settings, flow and transport are dominated by hydraulically connected fracture networks that create preferential pathways, enabling rapid contaminant migration while limiting the effectiveness of natural attenuation and engineered remediation strategies. At the same time, diffusion of contaminants into the low-permeability rock matrix can result in long-term storage and slow back-diffusion, prolonging plume persistence even after source removal.

TCE is particularly problematic in fractured bedrock because it can exist in multiple phases depending on subsurface conditions (National Research Council, 2005; Pankow & Cherry, 1996). Following release to the subsurface, TCE is typically introduced as a DNAPL, which then undergoes dissolution into the aqueous phase, volatilization into the gas phase in the vadose zone, and sorption to the solid matrix while migrating as a separate phase and/or within the water and gas phases. DNAPL TCE can migrate downward through fractures under gravity, bypassing much of the surrounding rock matrix and accumulating at depth. In addition to these advective processes, molecular diffusion transfers TCE from fracture networks into the low-permeability rock matrix, creating a long-term reservoir that slowly releases contamination back to the fractures (Neretnieks, 1980; B. L. Parker et al., 2008).

Even when DNAPL is no longer present, dissolved phase contamination in the matrix pores can continue to act as a long-term secondary source, sustaining groundwater and soil gas contamination for decades. These multiphase and multiscale processes significantly complicate both conceptual site models and quantitative predictions of contaminant behavior (Chapman & Parker, 2005).

Traditional remediation approaches, such as pump-and-treat systems, are often ineffective in fractured bedrock due to limited hydraulic connectivity between fractures and extraction wells, as well as slow mass transfer from the rock matrix (Mackay et al., 2000; National Research Council., 1994). Bedrock vapour extraction (BVE) is a technology, designed to remove volatile contaminants by inducing gas-phase flow through fractured rock (Ho & Webb, 2006). By lowering subsurface vapour pressures, BVE promotes volatilization of contaminants and enhances mass removal from fractures and surrounding pore spaces. However, the performance of BVE systems is highly site-specific and depends on factors such as fracture connectivity, moisture distribution, permeability contrasts, and operational design.

Given the complexity of fractured bedrock systems, numerical modelling has become an essential tool for supporting site characterization, remediation design, and performance evaluation (Bear et al., 1993; National Research Council, 2005). Advanced multiphase flow and transport models allow for the integration of geological, hydrological, and chemical data within a consistent mathematical framework. When properly configured and validated against field observations, such models can improve conceptual understanding of contaminant behaviour, identify dominant transport pathways, and support decision-making for remediation optimization. Nevertheless, modelling fractured systems remains challenging due to uncertainties in fracture properties, scaling issues, and the need to balance model complexity with computational feasibility. Given the complexity of fractured bedrock systems, numerical modelling has become an essential tool for supporting site characterization, remediation design, and performance evaluation (Bear et al., 1993; National Research Council, 2005). Advanced multiphase flow and transport models allow for the integration of geological, hydrological, and chemical data within a consistent mathematical framework. When properly configured and validated against field observations, such models can improve conceptual understanding of contaminant behaviour, identify dominant transport pathways, and support decision-making for remediation optimization. Nevertheless, modelling fractured systems remains challenging due to uncertainties in fracture properties, scaling issues, and the need to balance model complexity with computational feasibility.

In recent years, numerical simulators capable of explicitly representing fracture–matrix interactions and multiphase processes have been increasingly applied to contaminated bedrock sites. For instance, the TOUGH3 code (Jung et al., 2017) has been extensively used to simulate multiphase flow in fractured reservoirs, particularly for CO2 and contaminant migration. CompFlow Bio with fractures (CFBioF) is one such simulator, offering the capability to model coupled air–water–contaminant flow and transport in porous and fractured media (Forsyth, 1994; Unger et al., 1995; Walton, 2013). Its ability to incorporate discrete fracture representations, equilibrium phase partitioning, sorption, first-order decay as a representation of “degradation”, and site-specific boundary conditions makes it well-suited for investigating vapour-phase remediation processes in fractured porous bedrock environments. However, applications of such models must be carefully evaluated against field data to ensure their reliability and practical relevance.

Motivated by these challenges, this thesis focuses on the numerical modelling of TCE NAPL flow and contaminant transport in mobile gas and water phases and vapour-phase remediation in fractured bedrock at the Component Test Laboratory III (CTL-III) area of the Santa Susana Field Laboratory. By integrating site-specific geological information, historical contamination data, and results from a recent BVE pilot test, the study seeks to enhance understanding of TCE behaviour in the vadose zone over several decades and to evaluate the effectiveness of BVE as a remediation strategy.

This research was conducted through a two-stage modelling framework. In the initial stage, referred to as the contamination phase, the model was developed and validated using observed field data to ensure its ability to accurately reproduce site-specific conditions seven decades after contamination began. Subsequently, the remediation phase was simulated by incorporating the BVE process under operating conditions consistent with those implemented during the field test. In this stage, the model results are compared against field measurements collected during BVE operation. This approach provides a coherent linkage between contamination characterization and remediation performance assessment.

1.2 Site Characterization

The Santa Susana Field Laboratory (SSFL), located in southeastern Ventura County, California, lies within a geologically complex region characterized by faulted and fractured bedrock, including interbedded sandstones and shales of the Cretaceous Chatsworth Formation (MWH, 2004). Extensive tectonic fracturing has created significant secondary porosity, which serves as preferential pathways for fluid (gas, NAPL and/or groundwater) flow and contaminant migration (SSFL Groundwater Advisory Panel, 2009). The site's hydrogeology includes both unsaturated and saturated fractured bedrock zones; while the primary porosity of the rock matrix exists, its low hydraulic conductivity makes bulk fluid movement highly dependent on fracture connectivity (Sterling et al., 2005).

Soil cover is generally thin, ranging from less than 0.3 m to 4.6 m across most of the site, consisting of weathered Chatsworth Formation materials and alluvium (Stantec, 2021). Historical industrial practices, including the extensive use of chlorinated solvents such as TCE for flushing rocket engines from the 1950s through the 1980s, led to widespread contamination. Large volumes of TCE were used in open-air test stands, often allowing fluids to infiltrate thin soils and migrate into the fractured bedrock (CH2MHILL, 2008). This dual-domain fractured bedrock system—rapid flow through fractures and slow diffusion into the rock matrix—creates complex DNAPL flow and transport behaviour. TCE as a solute in the aqueous and gas phases readily migrates through fractures but diffuses into the surrounding porous matrix, resulting in long-term residual contamination and sustained back-diffusion from the matrix into flowing groundwater (Pankow & Cherry, 1996; B. L. Parker et al., 2012). Consequently, the matrix acts as a persistent secondary source even after primary source removal, posing a significant challenge for remediation (Chapman & Parker, 2005). Figure 1 shows the location of the CTL-III study site within the SSFL in Ventura County, California. The BVE experimental site extends horizontally to a radius of approximately 76 m from the central well (RD-46A). Vertically, the effective treatment zone ranges from about 9 to 23 m below ground surface,

corresponding to a thickness of roughly 14 m. This interval largely overlaps with the primary fractured zone, which spans from approximately 7.5 to 24 m below ground surface (Jacobs, 2025). The map illustrates the spatial distribution of the extraction well (RD-46A), and monitoring wells (BV-1, BV-02, BV-3, and C-33) relative to the local topography.

High-resolution characterization at the study site demonstrated that a substantial portion of the remaining TCE mass resides in the vadose zone and shallow fracture network near the RD-46A/RD-46B well pair, rather than exclusively within the saturated zone. Core hole RD-46B showed elevated porewater TCE up to ~100 mg/L, primarily between 9 to 21 m below ground surface within a moderately fractured interval (23 fractures logged from ~7.5 to 24.2 m bgs), indicating significant mass storage and potential for vapour phase migration in unsaturated fractured sandstone of the Chatsworth Formation (depth to groundwater ~26.8 m bgs). These findings, together with site history pointing to releases from the Module 3 test stand and the unlined CTL-III pond, provided a clear rationale to evaluate a vadose zone–focused remedy.

Accordingly, a BVE Pilot Test was initiated at CTL-III, repurposing RD-46A as the extraction well and installing a network of multilevel vapor monitoring wells to quantify vacuum propagation, advective gas removal from connected fractures, and diffusion limited back release from the partially water-saturated rock matrix are key performance metrics needed to assess BVE effectiveness in fractured bedrock and to inform subsequent corrective measures decisions (Jacobs, 2025).

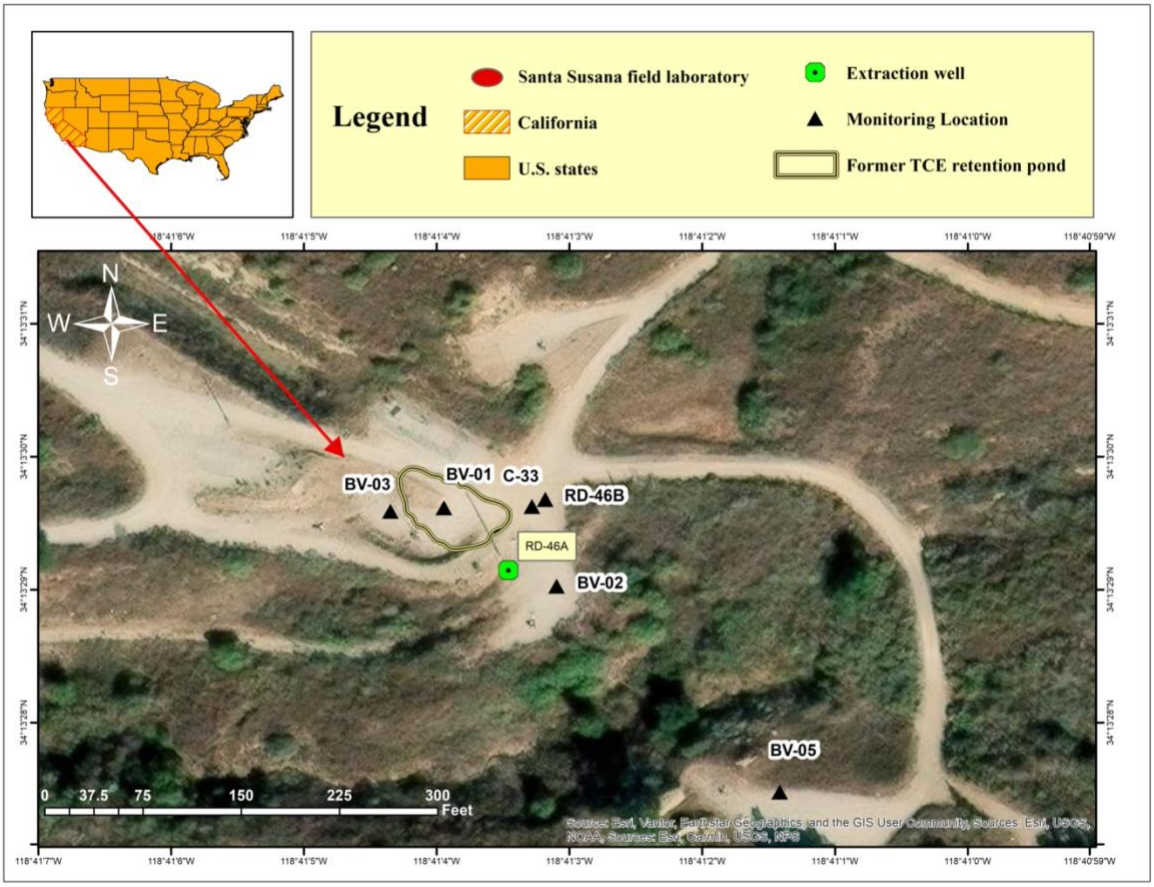


Figure 1 : Aerial view of the CTL-III and BVE Pilot Test area, including locations of cored holes/monitoring wells, and BVE extraction well. Inset: Location of the Santa Susana Field Lab in the state of California, USA.

1.3 Objectives and Scope

The primary objective of this research is to develop a robust numerical modelling framework to simulate TCE contaminant transport within the complex fractured bedrock of the CTL-III site at the SSFL. This work is fundamentally driven by the need to bridge the gap between theoretical transport physics and the practical realities of a large-scale, high-stakes environmental remediation project (MWH, 2009). Central to this study is the high-fidelity modelling of an actual BVE test conducted at the SSFL. Unlike idealized laboratory experiments, this research focuses on replicating the unique geological and hydrogeological responses observed using high-resolution characterization and monitoring data during live field operations as documented in the pilot test reports.

To achieve this objective, this study investigates and quantifies the mechanisms of TCE migration within a dual-porosity environment. This includes accounting for the interplay between high but variable conductivity fracture networks and the lower-permeability rock matrix, a process often governed by matrix diffusion (B. L. Parker et al., 2012). By evaluating

the performance of BVE as a remedial strategy, this research seeks to determine the area of influence of the extraction wells and the mass removal efficiency of Volatile Organic Compounds (VOC) from the unsaturated zone. Furthermore, a sensitivity analysis of hydrogeological parameters is conducted to identify the critical variables, such as fracture aperture and connectivity (affected by fracture length), that most significantly impact the accuracy of the transport model at the SSFL site.

This research is unique as it represents the first instance of applying comprehensive numerical simulation to this specific field data set from CTL-III. While previous studies have addressed fractured bedrock or vapour extraction in isolation, the integration of real-world site data from the SSFL into a predictive model provides a novel contribution to the field of contaminant hydrogeology. Modelling a "real test" introduces complexities that are often absent in academic simulations. The heterogeneity of the Chatsworth Formation and the historical magnitude of the TCE contamination at SSFL provide an unprecedented opportunity to validate simulation techniques against empirical data. By achieving a calibrated model that reflects real field conditions, this research provides a template for future remediation efforts at similar fractured bedrock sites worldwide.

The scope of this thesis is specifically focused on the CTL-III area of the Santa Susana Field Laboratory, encompassing an analysis of historical TCE concentration data and geological logs from the site (Hurley, 2003; MWH, 2004; Sterling & Parker, 1999). The work involves the development of a conceptual model that simplifies the fractured bedrock into a computationally manageable yet representative system, followed by the execution of numerical simulations focusing on the unsaturated (vadose) zone where BVE is most active. Finally, a comparative analysis is performed between the simulation results and the measured data from the actual BVE field test. This research does not intend to model the entire SSFL site-wide plume but rather focuses on the localized dynamics of the CTL-III BVE pilot test to ensure a high degree of precision and detail in the transport analysis.

1.4 Thesis Organization

This document is organized into five distinct chapters to systematically present the research. Chapter 1 introduces the background, site description, and the specific objectives and scope of the study. Chapter 2 provides a comprehensive literature review, examining current theories on fractured rock hydrogeology, TCE migration mechanisms in NAPL, gas and aqueous phases, and the state of vapour extraction technologies. In Chapter 3, the methodology is detailed, describing the conceptual model development, the selection of numerical codes, and the calibration process used to simulate the field test. Chapter 4 presents the results of this research, covering both the contamination phase and the subsequent remediation phase to evaluate model accuracy. Finally, Chapter 5 provides a summary of the major findings and discusses the implications of the results.

Chapter 2
Literature Review

2.1 Site-Specific Hydrogeology of the Santa Susana Field Laboratory (SSFL)

Research specific to the Chatsworth Formation at SSFL characterizes it as a dual-porosity system where structural geology dictates contaminant fate. (Montgomery-Watson, 2000) conducted extensive field mapping that categorized the site's fractured sandstone as having high matrix porosity but low matrix permeability, a combination that favours the sequestration of TCE. While Sterling et al. (2005) utilized high-resolution vertical profiling to map the heterogeneity of these plumes, SSFL Groundwater Advisory Panel (2009; 2020) synthesized decades of site data to argue that the bulk of the TCE mass at SSFL has transitioned from the liquid phase to the dissolved and sorbed phases within the rock matrix. This body of work establishes that any remediation strategy at CTL-III must account for the specific fracture frequency and bedding planes unique to the Santa Susana site.

2.2 Theoretical Framework of DNAPL in Fractured Media

The conceptual understanding of TCE in fractured bedrock has evolved from simple conduit flow models to complex matrix-interaction theories. Early foundational work by Kueper & McWhorter (1991) established the physical requirements for DNAPL entry into fractured media, emphasizing that capillary pressure dictates migration patterns. However, the paradigm shifted significantly when Parker et al. (1994) and Pankow & Cherry, (1996) introduced the concept of matrix diffusion, arguing that TCE does not remain in the fractures but rather diffuses into the stagnant pore space of the surrounding rock reasonably fast. The consequence was further advanced by (Parker & McWhorter, 1994; Wilson, 1996). Lipson et al., (2005), who demonstrated that even if the fractures are flushed, the matrix acts as a long-term secondary source through back-diffusion. This evolution highlights a critical challenge for the current research: the bedrock at CTL-III is likely not just a pathway, but a massive reservoir of historical mass.

2.3 Challenges in Applying Vapour Extraction

Soil vapour extraction (SVE) has been widely applied since the early 1980s as a primary remediation technology for VOC contamination in the vadose zone. The technique was originally developed to limit the downward migration of contaminants to underlying groundwater by inducing advective air flow through permeable, unconsolidated soils, thereby promoting volatilization and removal of contaminant mass (Hutzler et al., 1989; Pedersen & Curtis, 1991).

At complex sites characterized by fractured or porous sedimentary bedrock—such as the Chatsworth Formation at the SSFL the effectiveness of conventional SVE is often limited. This reduced performance is primarily attributed to preferential airflow through discrete fracture networks and the retention of contaminant mass within the low-permeability rock matrix, where mass transfer is governed by slow molecular diffusion rather than advective flow (Parker et al., 1994; SSFL Groundwater Advisory Panel, 2009). To overcome these limitations, BVE

was developed as a specialized adaptation of SVE for fractured rock environments. Unlike traditional SVE systems, BVE employs strategically placed boreholes designed to intersect targeted fracture networks, enabling more direct recovery of vapor-phase contaminants from the contaminated bedrock mass (USACE, 2002).

Previous studies have shown that BVE can effectively reduce vapor-phase contaminant mass in both fractured sedimentary and crystalline bedrock settings. This reduction can lower contaminant mass flux to groundwater and decrease the potential for vapor intrusion. However, long-term performance is often constrained by factors such as matrix diffusion and limited fracture connectivity, which can restrict sustained mass removal (NASA, 2015). System performance is particularly sensitive to the kinetics of matrix back-diffusion, a process that commonly results in contaminant concentration rebound following system shutdown (Chapman & Parker, 2005; Lipson et al., 2005). In addition, moisture conditions within the bedrock play a critical role, as elevated water saturation can reduce gas-filled porosity and inhibit vapor-phase mass transfer by isolating contaminants from induced advective airflow (EPA, 2001; Yoon et al., 2002). Consequently, remediation strategies for fractured bedrock increasingly integrate BVE with enhancement techniques such as thermal treatment, pulsed extraction, or hydraulic manipulation. These approaches are intended to mitigate diffusion-limited mass transfer, improve contaminant recovery, and enhance long-term protection of groundwater resources (EPA, 2001; ITRC, 2017)

2.4 Description of the CTL-III and BVE Pilot Test Areas

The pilot test system modelled in this study is based on a BVE field experiment conducted at the CTL-III area of the SSFL, California, which can be found in Figure 1. The pilot study was designed to evaluate the feasibility and effectiveness of BVE as a remediation technology for chlorinated volatile organic compounds, with TCE as the primary contaminant of concern, in unsaturated fractured bedrock. The test area is located in the southeastern portion of the CTL-III Resource Conservation and Recovery Act (RCRA) Facility Investigation site near the existing RD-46A/RD-46B well pair, an area with documented elevated TCE concentrations in the vadose zone porewater and moderate to intense bedrock fracturing (MWH, 2020; Stantec, 2021). The pilot BVE system utilizes an existing groundwater extraction well, RD-46A, which was temporarily retrofitted to function as a vapour extraction well. The well is completed to a depth of approximately 43 m below ground surface (bgs), with the groundwater table located at approximately 27 m bgs. Surface casing extends to a depth of approximately 9 m bgs, leaving a substantial open-hole interval within the unsaturated Chatsworth Formation sandstone available for application of vacuum and vapor extraction. This configuration allows induced airflow to propagate through interconnected fracture networks while minimizing disturbance to the saturated zone during system operation (Jacobs & Morwick G360 Groundwater Research Institute, 2022).

To monitor system performance and characterize subsurface responses, a network of observation and monitoring points was installed around the extraction well. This network includes a deep cored hole (C-33), five newly constructed multilevel system (MLS) vapor monitoring wells (BV-1 through BV-5), two shallow vapor monitoring wells completed in the

alluvium (BVS-2 and BVS-3), and one existing monitoring well (RD-149) modified for pressure and vapor monitoring. The MLS wells were drilled to depths ranging from approximately 34 to 38 m bgs and instrumented with flexible liner systems containing multiple depth-discrete monitoring ports. These ports enable measurements of vapor pressure, temperature, and CVOC concentrations in both fracture-dominated and matrix-dominated intervals of the vadose zone, providing detailed insight into fracture–matrix interactions during BVE operation (Jacobs & Morwick G360 Groundwater Research Institute, 2022).

The BVE pilot system includes a trailer-mounted vapor extraction and treatment unit powered by grid-supplied electricity. Vapor extraction is achieved using a positive displacement rotary claw blower capable of generating vacuums of up to approximately 68 kPa (equivalent to 20 inches of mercury), with a maximum flow capacity of about 4.2 m^3/min. Extracted vapours pass through a moisture separation unit to remove condensate prior to treatment, followed by a vapor treatment train consisting of multiple vapor phase granular activated carbon (VGAC) vessels arranged in series to ensure effective removal of CVOCs before atmospheric discharge. System operation includes continuous monitoring of applied vacuum, vapor flow rate, temperature, and contaminant concentrations to support both performance evaluation and regulatory compliance (Jacobs & Morwick G360 Groundwater Research Institute, 2022).System operation includes continuous monitoring of applied vacuum, vapor flow rate, temperature, and contaminant concentrations to support both performance evaluation and regulatory compliance (Jacobs, 2025).

The BVE pilot test was implemented over a total duration not exceeding ten months and included phases of baseline monitoring, active vapor extraction, and rebound testing. Active extraction periods were periodically interrupted by controlled system shutdowns to assess contaminant rebound attributable to diffusion from the bedrock matrix into fractures. Data collected during the pilot study include effluent gas phase TCE concentrations, contaminant mass removal estimates, vacuum propagation metrics, subsurface moisture conditions, and pressure responses over time (Jacobs & Morwick G360 Groundwater Research Institute, 2022).

These data form the basis for calibration and evaluation of the numerical model developed in this study and enable assessment of the model's ability to replicate observed field-scale BVE behaviour in fractured bedrock systems. phase concentrations, contaminant mass removal estimates, vacuum propagation metrics, subsurface moisture conditions, and pressure responses over time.

Chapter 3
Methodology

This chapter presents the methodological framework used to simulate contaminant transport and vapour-phase remediation in unsaturated fractured bedrock, with specific application to a field-scale BVE Pilot Test conducted at SSFL's CTL-III area. The approach employs the multiphase, multicomponent numerical simulator CFBioF (Forsyth, 1994; Unger et al., 1995; K. M. Walton, 2013) to represent coupled gas phase and aqueous phase flow and transport of TCE vapour and solute within a fractured and heterogeneous porous rock subsurface system. The modelling framework incorporates discrete fracture representations, capillary pressure and relative permeability relationships, and equilibrium phase partitioning to capture the key mechanisms governing TCE migration and removal in the vadose zone. Site-specific geological conditions and operational parameters from the BVE field test were used to configure the numerical domain, enabling simulation of both long-term contaminant evolution under natural conditions and transient system response during active remediation. Model performance was assessed through comparison of simulated results with field observations, allowing evaluation of the model's ability to reproduce observed contaminant distributions, moisture conditions, and fracture–matrix interactions. Overall, this methodology establishes a direct link between field-scale testing and numerical simulation to support understanding and assessment of remediation strategies in fractured bedrock environments (Figure 2).

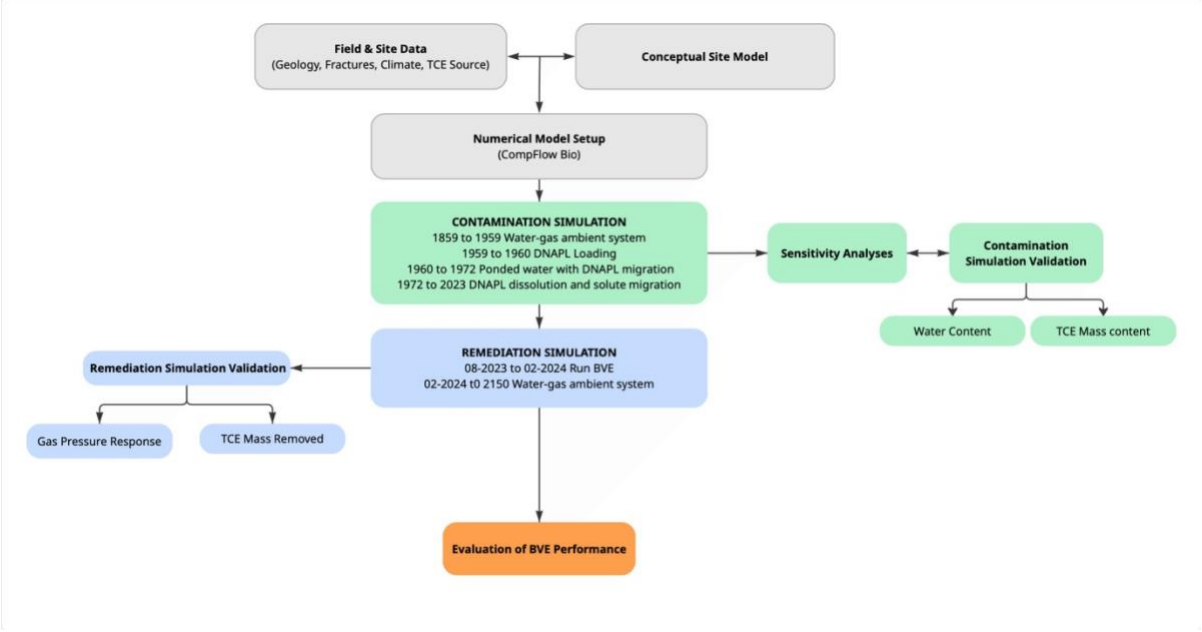


Figure 2 : Workflow for TCE modelling and BVE evaluation at CTL-III.

3.1 Conceptual Site Model

The conceptual site model used to represent the BVE pilot test is framed within a dual-porosity paradigm, which is fundamental to characterizing the transport and storage of TCE in fractured bedrock (Figure 3). In this framework, the Chatsworth Formation is represented as two distinct yet interacting porosities: a high-conductivity but low porosity network of tectonic fractures and a surrounding low-conductivity but higher porosity rock matrix. The fractures serve as the primary advective pathways, facilitating the rapid migration of fluid and gas phases over significant distances. Conversely, the sandstone matrix acts as a reservoir that sequesters the majority of the contaminant mass through matrix diffusion.

The subsurface conditions at CTL-III, described by Jacobs (2025) is summarized as follows: A thin veneer of alluvium and weathered bedrock, typically ranging from 0.3 to 4.6 meters in thickness, overlies the competent Chatsworth Formation (MWH, 2004). The conceptual site model domain focuses on the thick unsaturated (vadose) zone, which extends approximately 27 meters (88 feet) to the water table. The schematic of the domain incorporates these vertical stratigraphic features, including the presence of lower-permeability siltstone and shale interbeds that influence the pneumatic connectivity of the system. A retention pond existed at the CTL-III area that captured TCE-laden process water discharged from the adjacent industrial operations (Walton et al., 2025). This spatial configuration allows for a detailed simulation of BVE, mapping how induced pressure gradients mobilize vapours through the fracture network while drawing dissolved-phase mass from the dense rock matrix.

Extraction well RD-46A is a 42.67 m-deep, 0.159 m (6¼-inch) diameter open borehole with steel surface casing to 8.99 m below ground surface (bgs) and an uncased interval from 8.99 to 42.67 m bgs, allowing direct hydraulic and pneumatic connection to both the fracture network and the surrounding sandstone matrix (Jacobs, 2025).

Geophysical and coring results show that RD-46A cuts dominant fracture sets with the primary vapour-producing fracture zone at ~11.28–13.11 m bgs, where flow logging identified the greatest air flux and TCE mass withdrawal. The water table was measured at 22.66 m bgs before extraction, so the well's open interval spans the vadose zone, capillary fringe, and the upper saturated zone, enabling applied vacuum to propagate through interconnected fractures and to drive diffusive mass transfer from the water-saturated rock matrix toward the fractures (Jacobs, 2025). The model domain is specifically designed to analyze these mass transfer rates, providing a quantitative basis for evaluating the radius of influence of extraction wells and the long-term efficiency of mass removal across the site's heterogeneous stratigraphic layers.

Figure 3 contrasts the contamination and remediation phases by showing the time-varying boundary conditions that drive the model. Across the domain, a steady precipitation recharge of 18 mm yr^{-1} is applied as $R_{ambient}$ while over the ponded area the model superposes focused pond infiltration of ≈ 2 mm d^{-1} during 1959–1972 as $R_{\text{pond}}(t)$, and a short-lived TCE input of ≈ 0.11 mm d^{-1} during 1959–1960 as $Q_{NAPL}(t)$. In the remediation panel, a time-dependent vacuum $P_{BVE}(t)$ is applied at the wellbore feature; the top boundary remains a free-gas

exchange surface, so the applied vacuum preferentially propagates through connected fractures and induces matrix-to-fracture diffusive mass transfer as gas concentrations are lowered.

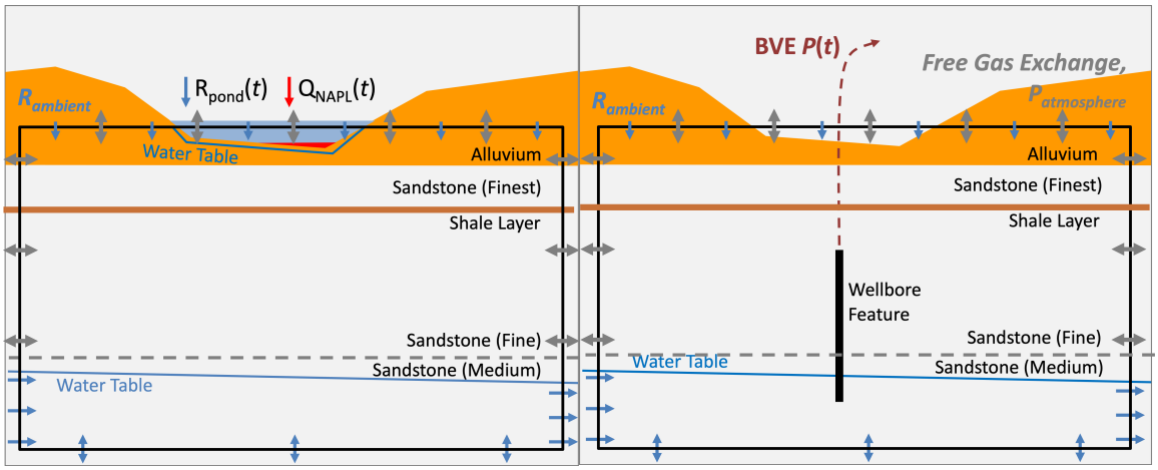


Figure 3 : Schematic of the subsurface lithologic of layers in the model domain (black outline) and applied boundary conditions, including surface flux, $R_{ambient}$ and $R_{pond}(t)$, NAPL loading, $Q_{NAPL}(t)$, gas exchange (gray arrows), water table position and hydraulic gradient (blue arrows). The left panel shows the boundary conditions that were considered during epoch 1, 2 and 3 (legacy contaminant transport modelling) and the right panel shows boundary conditions that were considered during epoch 4 and 5 (BVE remediation modelling).

3.2 Subsurface Material Properties at CTL-III

The proposed geometry and stratigraphic framework for the conceptual model of the BVE Pilot Test area was developed based on the interpretation of gamma-ray (GR) logs from boreholes BV-1, BV-3, and C-33 (Figure 4). Analysis of the GR profiles enabled delineation of three primary lithologic units within the model domain: surficial alluvium, finer-grained sandstone, and medium-grained sandstone. The vertical extent of these units and their depth intervals are summarized in Table 1, which presents the stratigraphic framework. Elevated GR responses are indicative of fine-grained lithologies, including shale and siltstone, whereas lower GR values correspond to sandstone units characterized by higher permeability (MWH, 2004; SSFL Groundwater Advisory Panel, 2009; Weaver et al., 2024). Within the finer-grained sandstone sequence, a thin shale layer was identified based on consistently high GR values and abrupt vertical transitions. This shale unit represents a laterally continuous, low-permeability interval that functions as a capillary and hydraulic barrier, restricting vertical migration of fluids and vapours. Such fine-grained layers are known to promote sorptive retention and matrix diffusion, contributing to long-term contaminant storage in fractured bedrock systems (Hurley, 2003).

The discrete fracture network (DFN) for the conceptual model of the BVE pilot system area was informed by field observations from core logging, geophysical surveys, pressure monitoring, and downhole flow profiling. Field observations from core holes reveal the depth, number, and spacing of fractures—such as the 23 fractures identified between 24.5 and 79.5 ft bgs in RD-46B—which directly define fracture density and vertical distribution. Televiewer

and NMR logs refine these observations by capturing fracture orientation, aperture, continuity, and transmissivity, enabling accurate representation of fracture geometry and connectivity. Pressure data from MLS wells show how vacuum propagates through connected fractures, establishing lateral connectivity and anisotropy of the network. PneuLog flow measurements in RD-46A identify which fractures actively transmit vapor and contaminant mass, supplying fracture-specific transmissivity and flux parameters. Concentration data from vapor, porewater, and core samples indicate where CVOC mass is stored in fractures versus the rock matrix, supporting estimates of matrix diffusion and mass-transfer rates. Together, these observations define the geometry, connectivity, transmissivity, and mass-exchange properties that form the basis of the site-specific fracture network model.

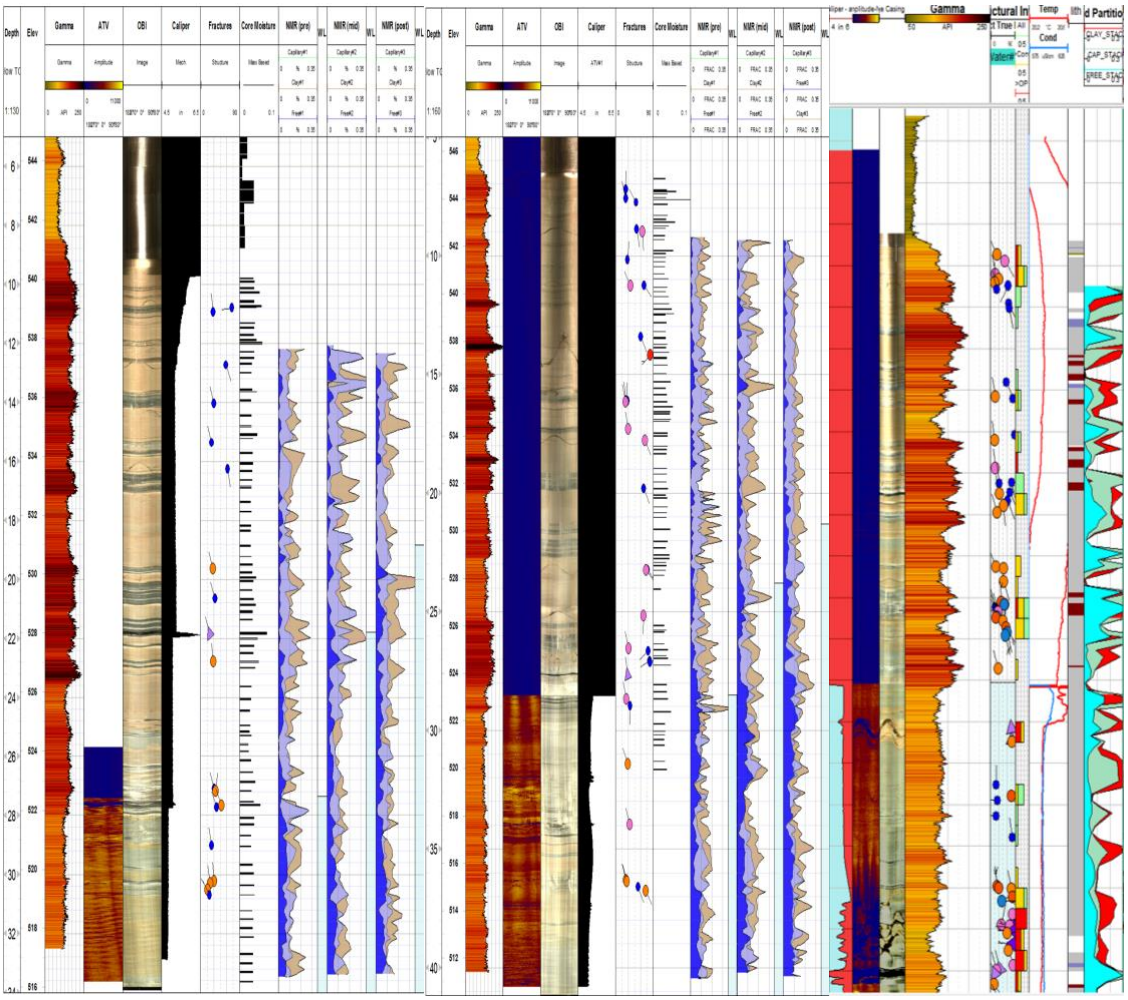


Figure 4 : BV-1, BV-3 and C-33 rock core moisture content and NMR (Figure 6,9 and 17 of Manna et al., 2025) .

Table 1 : Summary of hydrogeological and geochemical model input parameters for contaminant transport simulation.

Parameter	Value	Comment	Reference(s)
Permeability			(Manna et al. 2019) (J. Hurley 2003)
Alluvium	2×10^{-13} m^2	Isotropic	
Fine Alluvium (Pond Lining/Bottom)	1×10^{-15} m^2	Isotropic	
Finer-Grained Sandstone (z=27.3-34 m)	7.5×10^{-15} m^2	15:1 K_h: K_v	
Shale (z=27-27.3 m)	2.5×10^{-18} m^2	10:1 K_h: K_v	
Finer-Grained Sandstone (z=10-27 m)	1.4×10^{-14} m^2	15:1 K_h: K_v	
Medium-Grained Sandstone (z=0-10 m)	1.8×10^{-14} m^2	15:1 K_h: K_v	
Porosity, φ			(Manna et al. 2019) (J. Hurley 2003)
Alluvium	0.3		
Fine Alluvium (Pond Lining/Bottom)	0.35		
Finer-Grained Sandstone (z=27.3-34 m)	0.145		
Shale (z=27-27.3 m)	0.06		
Finer-Grained Sandstone (z=10-27 m)	0.145		
Medium-Grained Sandstone (z=0-10 m)	0.13		
Sorption			(Hurley, 2003)
Alluvium		R = 0	
Sandstone bulk density, $\boldsymbol{r_b}$	2280 kg/m^3	R =1.31-1.34	
Sandstone, $\boldsymbol{f_{oc}}$	0.00021	R = 10.3	
Shale bulk density, $\boldsymbol{r_b}$	2280 kg/m^3		
Shale, $\boldsymbol{f_{oc}}$	0.0026	R = 10.3	
Dry Bulk Density			(Hurley, 2003)
Lower bound value Median (simulated) Upper bound value	2160 kg/m^3 2280 kg/m^3 2390 kg/m^3		
Fracture Network			(Bairos et al., 2023)
Horizontal Fractures, $P_{10,z}$	0.909 /m	Counts/Distance	
Vertical Fractures, $P_{10,x}$	0.928 /m	Counts/Distance	
Geometric Mean Aperture	94 μm		
Log-normal Aperture Distribution Variance	1.6e-8 m^2		
Fracture porosity, P_{33}	0.00025	V_{void}/V_{bulk}	
TCE Properties			
Organic Carbon Distribution Coeff., $\boldsymbol{K_{OC}}$	0.094 m^3/kg		(Hurley, 2003)
First-order Decay Half-Life, $t_{1/2}$	20 yr		(Yu et al., 2020)

3.3 Numerical Model

The selection of a numerical simulator for modelling transport and remediation in fractured bedrock requires a code capable of handling complex multiphase flow, solute transport, and discrete geological features. For this research, the CFBioF numerical modelling software was selected. This simulator is a robust, multicomponent, three-phase (water, gas, and non-aqueous phase liquid) code that has been documented in academic literature for its performance in simulating subsurface contaminant dynamics, such as those involved in BVE (Forsyth, 1994; Unger et al., 1995; K. M. Walton, 2013; K. M. Walton et al., 2019). CFBioF operates on the fundamental assumption of laminar, Darcian flow for both the aqueous and gas phases. It is particularly well-suited for this study as it was specifically developed to simulate the remediation of NAPLs through various engineered strategies, such as air sparging and soil vapour extraction (Forsyth, 1994; Unger et al., 1995). Moreover, the CFBioF code incorporates discrete fracture into the computational domain (Walton, 2013). This capability is essential for the SSFL site, where fracture-controlled flow is the dominant mechanism for both contaminant migration and vapour recovery.

To maintain numerical efficiency while preserving physical realism, several simplifying assumptions were adopted. Flow in both aqueous and gas phases is governed by Darcy's law, with laminar flow assumed throughout the domain. The influence of fractures is represented explicitly in CFBioF through discrete fracture control volumes that capture their geometry and hydraulic behavior, consistent with the scale of the pilot test and available site-specific data. These assumptions are consistent with prior applications of CFBioF and are appropriate for pilot-scale simulations in heterogeneous sedimentary environments. In the following section, field data from the SSFL and BVE pilot test will be incorporated to construct the computational domain and assign site-specific hydrogeologic and biogeochemical properties.

3.3.1 Computational Domain and Boundary Conditions

Representative simulation of fluid flow and contaminant transport in the fractured bedrock of the SSFL requires a computational approach that explicitly accounts for the extreme physical heterogeneity of the system. This heterogeneity is primarily defined by the contrast between the low-permeability rock matrix and the network of low-volume, high-conductivity fractures. To capture this complex behaviour, a discrete fracture-matrix (DFM) approach was adopted. See Berre et al. (2019) for alternative approaches for the simulation of fractured porous rock. The simulation domain, corresponding to the CTL-III area of interest, was discretized using a control volume finite difference (CVFD) method. The computational CVFD grid consisted initially of 124 porous medium cells in the horizontal direction and 81 cells in the vertical direction (where cells may be further subdivided to accommodate discrete fractures), resulting in a pseudo 2-D representation of the fractured system. Cell sizes in both the horizontal and vertical range from 0.1 m to 1.0 m, with the finest resolution (0.1 m) applied in regions near lateral domain boundaries. The model employs a non-uniform vertical discretization scheme to better resolve key hydrogeological processes across stratigraphic layers. As illustrated in Figure 5a, grid refinement is highest near critical interfaces, including the ground surface, the infiltration pond region, and the shale layer. These zones are discretized more finely to

accurately capture steep hydraulic gradients, phase interactions, and mass transfer processes. In contrast, coarser vertical discretization is applied within relatively homogeneous units such as the central portions of the upper and lower bedrock, where gradients are less pronounced and flow conditions are more uniform. The alluvial layer also exhibits finer discretization near the surface to better represent infiltration dynamics and near-surface transport processes. Additionally, increased resolution is evident near the transition to the saturated zone, allowing for improved representation of capillary effects and vertical flux exchanges across the water table. This targeted refinement strategy ensures computational efficiency while maintaining high accuracy in regions where physical processes are most sensitive to vertical variability.

The DFM architecture explicitly represents the bedrock fractures as a set of interconnected planar features (Figure 5b) that provide preferential pathways for advective transport of groundwater and vapour due to their relatively high permeability. The surrounding rock mass is represented as a connected porous media domain that participates in multiphase flow while also serving as the primary storage domain for contaminant mass through slow matrix diffusion (Sudicky & McLaren, 1992). Representing both fracture and matrix domains explicitly allows the model to simulate coupled multiphase flow and transport processes, including advective movement through fractures and the slower diffusive exchange and storage within the rock matrix, which are key mechanisms controlling long-term TCE persistence and the response to the pilot BVE remediation exercise. Discrete fractures are represented by distinct 2-D CVFD entities, where the third dimension, aperture, is a property of each fracture control volume; fracture intersections are subject to algebraic elimination from the matrix-vector system of equations as described in (Walton et al., 2019). 3-D PM control volumes that are separated by at 2-D fracture volume maintain a 10% contact area as described in (Walton, 2013, Figure 2-2 and Appendix C), which effectively reduces the capillary barrier effect of air-filled fractures on downward infiltration of water through the matrix. This resulted in the computation domain depicted in Figure 5 containing 9658 fracture control volumes and 13371 PM control volumes.

Based on the core logs shown in Figure 4, the stratigraphy beneath the surficial alluvium was further resolved for the purposes of specifying the properties of the computational domain as depicted in Figure 5c. Specifically, fine-grained alluvium was utilized as lining for the infiltration pond. Next, the sandstone unit was placed beneath the surficial alluvium. This sandstone unit was subdivided into an upper finer-grained subunit underlain by a medium-grained subunit. The thickness of these stratigraphic units follows from Table 1. Finally, a shale layer was placed within the upper fine-grained alluvium. Each stratigraphic unit is represented as a homogeneous porous medium, with uniform properties assigned within individual layers as summarized in Table 1. Lateral continuity of stratigraphic units is assumed within the modelled domain, which is a simplification of borehole correlations that show a 25º dip angle. The domain is two-dimensional, 40 m high, 120 m long and with a unit width of 1 m. The water table is located at an approximate elevation of 6 m with respect to the datum.

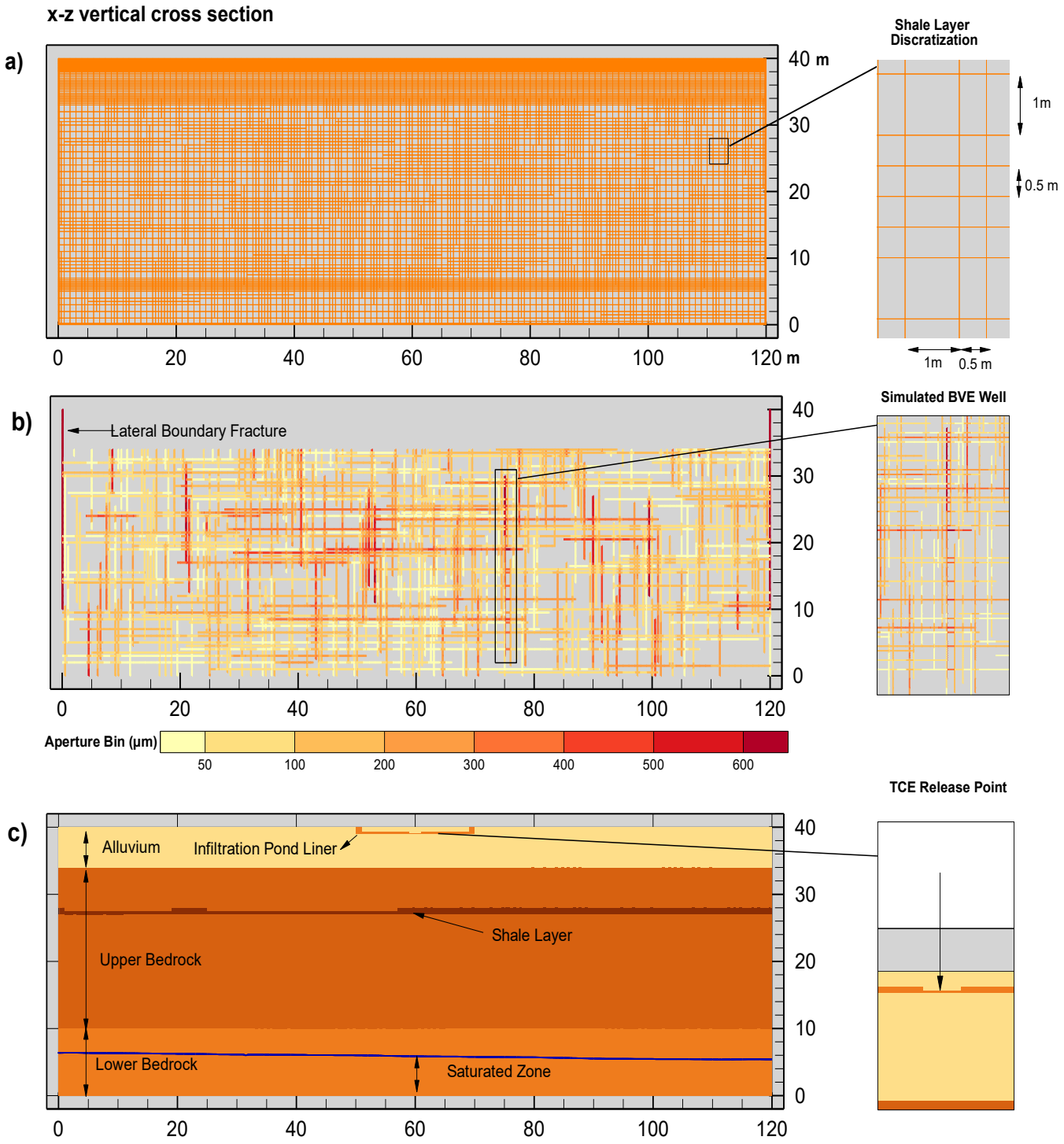


Figure 5 : a) Discretization of the PM. b) DFN used to inform numerical discretization. The 2-D x–z section displays fractures colour-mapped by aperture length, with warmer tones indicating wider aperture and higher transmissivity. c) Multi-layered lithologic units interpreted from Gamma-Ray data.

The statistical characteristics of the DFN were based on fracture data derived from borehole imagery and core observations. This fracture network (one realization) was stochastically generated based on the statistical parameters of the site (Jacobs, 2025), and the one realization depicted in Figure 5b. In total, there are 478 individual fracture planes with both horizontal and vertical orientations. The average horizontal fracture length is 25 meters, the average vertical length is 11 meters, and the log-normal mean aperture size is 0.13 mm. The aperture distribution is presented in Figure 6 (left panel). Furthermore, the vertical density of the network, including the cumulative count of one fracture per meter depth (P_{10}), is illustrated in Figure 6 (right panel). This DFN parameterization aligns with the known fracture architecture and hydraulic properties at the CTL-III site and provides a robust foundation for subsequent interpretation of BVE system performance (Manna et al., 2025; Walton, 2013).

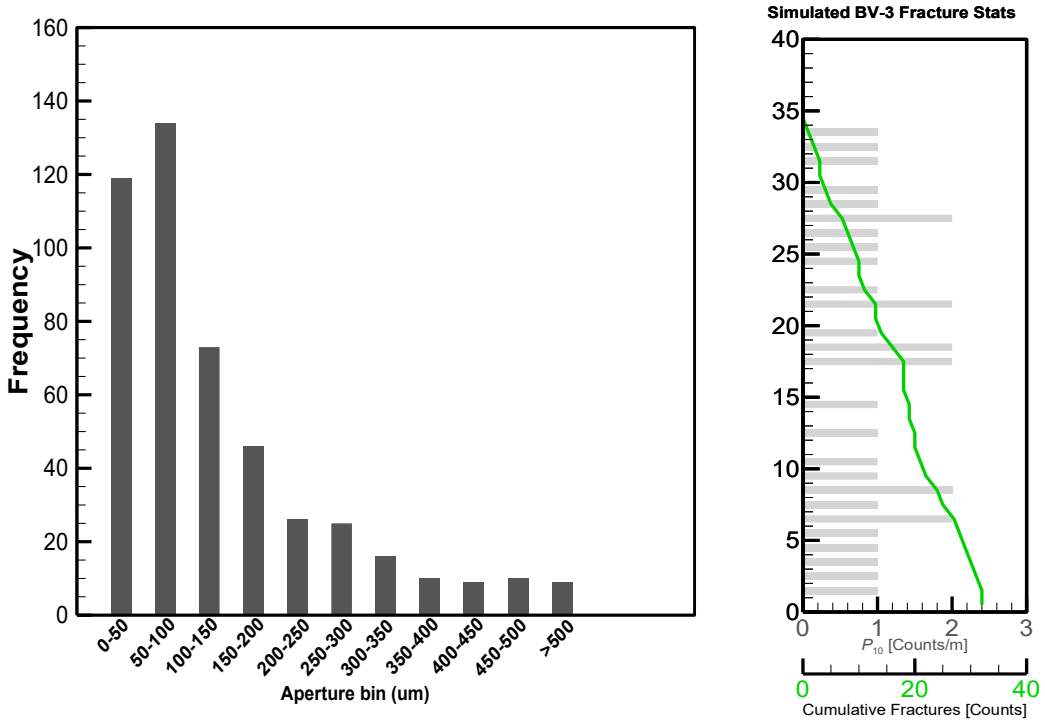


Figure 6 : Frequency distribution of fracture aperture sizes in the simulation's discrete fracture network (Left); Vertical Distribution and Cumulative Count of Fractures per Meter Depth (P_{10}) from the profile at x=60 m (right).

The boundary conditions illustrated in Figure 3 are implemented in the numerical model to ensure a physically consistent representation of flow and transport phenomena within both the vadose and saturated zones of the CTL-III site, in a sequence of five "epochs" as indicated in Figure 2. During all epochs, the lateral and top boundaries were configured to permit unrestricted gas exchange with the atmosphere, thereby enabling accurate simulation of gas-phase dynamics in the unsaturated zone in response to infiltrating water as well as during BVE. Two large aperture fractures are manually inserted near the x=0 and 120 m boundaries to create

a connection of the bedrock vadose zone with the atmosphere boundary condition at z=40 m; these facilitate a numerically robust, gravity drainage process from fully saturated initial conditions to variably saturated ambient conditions in the bedrock. Within the saturated zone, a mild lateral hydraulic gradient of 0.01 was introduced to approximate natural groundwater flow. During the first epoch, which ended in 1959, a constant flux of water at a rate of 40 mm/yr (Manna, 2023, personal communication) was prescribed at the upper boundary to simulate natural recharge and establish a steady-state water saturation within the vadose zone and water table elevation. Also, during this epoch, enhanced infiltration of pondwater was introduced into the domain via injection of water at a rate of 2 mm/day within the infiltration pond located at the top of the alluvium. The second epoch extends from 1959 to 1972. Initially, TCE was injected at a rate of 0.0001 m^3/day along with the pondwater from 1959 to 1961 only. Thereafter, clean pondwater continued to infiltrate until the end of the second epoch. During the third epoch from 1972 to 2023, enhanced infiltration of pondwater was stopped and the ambient recharge infiltration system was allowed to re-establish itself. During the fourth epoch from 2023 to 2024, a vacuum was imposed within the BVE wellbore (implemented as a large aperture fracture at x=75.05 m, from z=3 to 30 m), where the vacuum was created by a lower gas phase pressure within the well bore than the ambient atmospheric gas phase pressure. The lateral boundary fractures enable lateral flow of air from the surficial atmospheric boundary condition towards the BVE well, in addition to that flowing downwards through the alluvium. During the fifth epoch from 2024 onwards, the BVE activity ended and again the ambient system was allowed to re-establish itself.

3.3.2 Governing Equations and Multiphase Flow Properties

Numerical simulations were performed using CFBioF, a multiphase, multicomponent model that simulates the simultaneous transport of aqueous, non-aqueous, and gas phases. The simulator employs a first-order accurate finite-volume method for spatial discretization and a fully implicit scheme to solve for phase pressures, saturations, and component mole fractions. Mass transfer between phases is governed by equilibrium partitioning. To ensure numerical stability and efficiency, the nonlinear system is linearized via the Newton-Raphson method with CGStab acceleration and an adaptive time-stepping algorithm. Detailed mathematical equations implemented in the code are reproduced from (K. M. Walton, 2013).

The equation for conservation of moles of component species *p*, with other symbols defined in the List of Symbols, is:

$$\frac{\partial}{\partial t}\left[\phi \sum_{l} S_l M_l X_{pl} + \rho_b K_d M_q X_{cq}\right] = -\sum_{l} \nabla \cdot \left(M_l X_{pl} \vec{v}_l\right) + \sum_{l} \nabla \cdot \left(\phi S_l \mathbb{D}_l M_l \nabla X_{pl}\right) + Q_p \tag{3.1}$$

The Darcy velocity is given by:

$$\vec{v}_l = -\mathbb{K}\frac{k_{rl}}{\mu_l}(\nabla P_l - \rho_l g \nabla d) \tag{3.2}$$

And the dispersion tensor from (Sleep & Sykes, 1989) has the form:

$$\phi S_l \mathbb{D}_l = \alpha_L^l \vec{v}_l \delta_{IJ} + \left(\alpha_L^l - \alpha_T^l\right)\frac{\vec{v}_{lI}\vec{v}_{lJ}}{|\vec{v}_l|} + \phi S_l \tau D_l^* \delta_{IJ} \tag{3.3}$$

During the contamination epoch, when both TCE and water are injected into the infiltration pond, some NAPL forms resulting in a three-phase aqueous, gas and non-aqueous phase liquid system, requiring three-phase capillary pressure and relative permeability relationships to simulate its evolution. However, the NAPL never becomes sufficiently mobile to leave the infiltration pond and impact the vadose zone beneath, in keeping with field observations at the site. In fact, no NAPL has been observed at the site since monitoring began. Therefore, simulation of BVE only requires consideration of two-phase gas-aqueous capillary pressure and relative permeability relationships within the matrix and fracture control volumes.

Walton (2013, Appendix A) describes the multiphase flow parameters and datasets previously used for SSFL simulations. The matrix two-phase capillary pressure–saturation (P_c-S) curves and relative permeability (k_r-S) relationships used with the numerical model were derived from laboratory core data of the Chatsworth formation (Amirtharaj et al., 2011). Their study utilized Mercury Intrusion Porosimeter (MIP) on Chatsworth Formation (sandstone in the case of the numerical model shown on Figure 3) core samples (specifically sample C4-137 from the SSFL site) to quantify pore-throat geometry and drainage behaviour. By applying standard capillary pressure relationships to the raw intrusion data, the authors derived critical parameters—including air-entry pressure, pore-size distribution indices, and residual saturation. The 10^{-7} m data from this sample were fitted using Brooks–Corey functions, as depicted in Figure 7. These experimentally derived relationships served as the foundation for selecting and calibrating the model's constitutive capillary functions, ensuring that the simulation reflects site-specific porous media physics. For this study, the residual NAPL saturation for TCE within the matrix was set to 0.06 (Keller & Chen, 2003), while the residual water and gas saturations can be observed in Figure 7, which illustrates the saturation-dependent behaviour of capillary pressure and relative permeability. Residual saturations for water, gas, and NAPL within matrix control volumes are critical in defining irreducible fluid masses, influencing long-term contaminant persistence.

For fractures, the k_r-S and P_c-S relationships are derived from the work of Mendoza (1992), who performed numerical experiments of rough-walled fractures. Figure 7 depicts these relationships for a 100 micron fracture, which are scaled to fractures of different apertures as described in (Walton, 2013, Appendix A). Fractures have significantly lower capillary pressure than the Chatsworth formation matrix, meaning water is held with less tension and fractures will drain more easily; the contrast in capillary forces between the matrix and fractures ensures that within the vadose zone, water remains imbibed within the matrix.

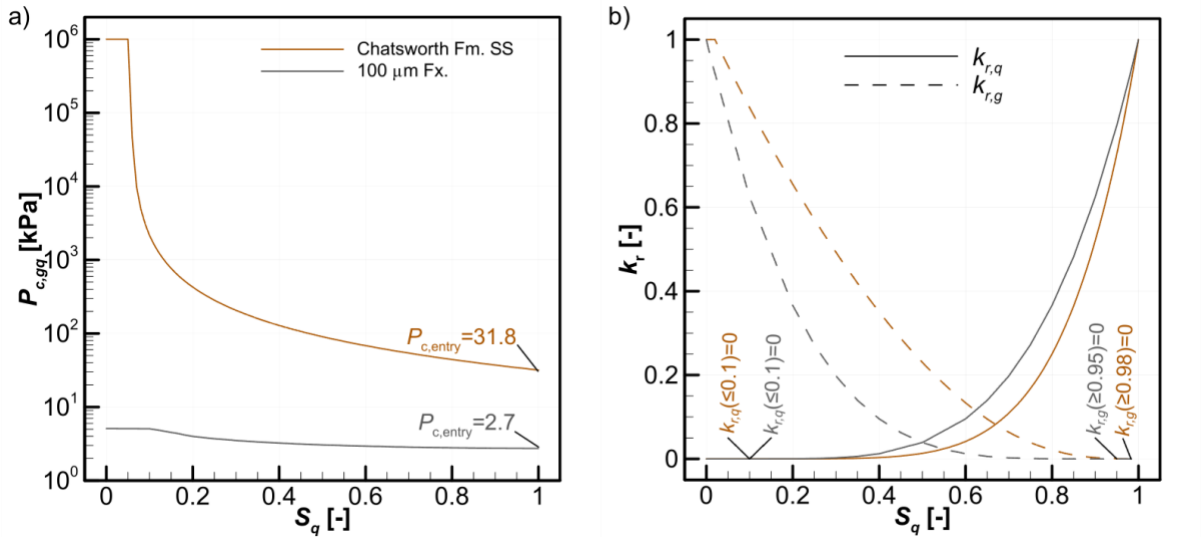


Figure 7 : Capillary pressure and relative permeability relationships for the Chatsworth formation matrix as well as for a 100-micron fracture.

3.4 Postprocessing of Numerical Model Outputs for Comparison to Field Data

To support a clear and consistent comparison between model predictions and field observations, all key postprocessing calculations used in this study are consolidated within this section. Here, the governing equations for moisture content, TCE mass content, dissolved-phase TCE concentrations, and other derived model outputs are presented together with the definitions of all associated variables and symbols.

3.4.1 Water Content

The water content was derived from simulation outputs of water saturation and porosity. The water content was calculated as:

$$WC = \frac{S_w \, \phi \, \rho_w}{\rho_b} \tag{3.4}$$

The quantities S_w and ϕ were obtained directly from the numerical simulation (and subject to spatial variability), while ρ_w and ρ_b were prescribed material properties.

3.4.2 TCE Concentration

The equations below formalize the procedure for translating model-generated mole fractions into mass-based concentrations for TCE. This conversion is necessary because field measurements are typically reported in units of mass per volume, whereas the numerical simulator tracks species composition in molar terms. By incorporating phase saturations and other parameters, the postprocessing method provides a complete representation of TCE mass distribution within each control volume and ensures that model predictions can be compared directly to observed site data.

$$C_{TCE,q} \cong X_{TCE,q} \cdot \rho_{M,water,q} \cdot M_{TCE} \tag{3.5}$$

Where the units are verified as follows:

$$\left[\frac{g_{TCE}}{m_q^3}\right] \cong \left[\frac{mol_{TCE}}{mol_q}\right] \cdot \left[\frac{mol_{water}}{m_{water}^3}\right] \cdot \left[\frac{g_{TCE}}{mol_{TCE}}\right]$$

The TCE mass fraction for all four phases (three fluid phases plus the sorbed phase) is calculated under the simplifying assumption of a dilute solution, i.e., $\text{mol}_q/\text{kg}_q \approx \text{mol}_{\text{water}}/\text{kg}_{\text{water}}$.

$$\text{Mass fraction} = \frac{C_{TCE,q}(\vec{x},t) \cdot S_q(\vec{x},t) \cdot \phi + m_{TCE,s}(\vec{x},t)/V_{CV}(\vec{x})}{\rho_{\text{bulk(dry)}}} \tag{3.6}$$

Here, $m_{TCE,s}$ is the mass of TCE in the sorbed phase within a control volume (CV), and V_{CV} is the volume of that CV. Mass contributions from the gas and non-aqueous phases are available but are either negligible or absent.

Chapter 4
Results

This chapter presents the results of numerical simulations performed to evaluate TCE transport and the effectiveness of BVE in unsaturated fractured bedrock, representing the BVE Pilot Test conducted at SSFL's CTL-III area. The simulation framework includes baseline scenarios representing the ambient air-water system, TCE NAPL contaminant loading to the pond, and dissolution and plume evolution under ponding and natural infiltration conditions, as well as remediation scenarios corresponding to the field-scale BVE test. Model outputs encompass spatial and temporal distributions of water content, gas pressure, and TCE mass in four phases (NAPL, gas, aqueous, and sorbed phases) within both fracture and matrix domains. In addition, the results quantify fracture–matrix interactions, the hydraulic and pneumatic response of the system to BVE operation, cumulative mass of TCE removed through vapour extraction, and TCE mass transmitted to groundwater. Where available, simulated results are compared with field observations to assess model performance, consistency with site-specific conditions, and consistency with Pilot Test outcomes.

A multi-stage numerical modelling strategy was adopted in this study to represent the temporal evolution of site conditions at CTL-III prior to and during implementation of BVE. The overall methodological workflow, including the relationship between the Contamination Simulation and Remediation Simulation stages, is illustrated in Figure 2. This approach was designed to ensure that remediation simulations were based on a physically realistic representation of pre-remediation subsurface conditions rather than assumed or simplified initial states.

A brief overview of the modelling workflow is provided here for context, with full details given in the Methodology chapter. The modelling workflow begins by simulating the temporal sequence of epochs 1, 2 and 3, as described in Section 3.3.1. Specifically, the model was used to simulate the transient evolution of the air–water system under ambient recharge and then ponded infiltration conditions, as well as the NAPL flow and the transport and fate of TCE in the aqueous and gas phases within the vadose zone (Figure 3a). The purpose was to establish the moisture and TCE distributions within the fracture–matrix system prior to bedrock vapour extraction (BVE). These simulated results were then evaluated by comparison to available field observations. The modelling workflow then proceeds by simulating epochs 4 and 5 as described in Section 3.3.1. Specifically, BVE is simulated using field-measured extraction rates and applied vacuum pressures from the pilot study in the CTL-III area (Figure 3b). Simulated responses were compared directly with field data to assess how well the model reproduced the performance of the BVE system and, therefore, can serve as a tool to interpret its efficiency.

4.1 Origin and Transport of TCE Contamination

4.1.1 Comparison of Simulated to Measured Water Distribution

Figure 8 presents the simulated spatial distribution of water saturations within the matrix and the discrete fracture network at the end of epoch 3 in 2023. The horizontal width of Figure 8

represents a geological cross-section that cuts across the CTL-III site and the BVE pilot test area. The vertical lines mark the positions of BV-3, BV-1, and RD-46B/C-33 along this cross-section, allowing the simulated water saturation distribution to be directly related to the physical well layout in the field. The left panel illustrates the two-dimensional distribution of aqueous-phase saturation in the matrix domain, while the right panels give depth profiles of water saturation, S_q, at simulation locations corresponding to BV-3, BV-1, and RD-46B/C-33. Parameters used in the CFBioF numerical model to simulate these water saturations are itemized in Table 1 and described throughout section 3.3.1.

Simulated water saturations depicted on the left graph of Figure 8 provides insight into the contrasting water retention behaviour of the Chatsworth Formation matrix and fracture features within the vadose zone, from elevations z = 0 to 34 m. The matrix exhibits relatively high and laterally continuous water saturation throughout much of the domain, with water saturation values generally exceeding 0.6 and approaching unity within the capillary fringe below elevation z = 10 m. This pattern reflects the strong water-holding capacity of the fine-grained bedrock matrix due to capillary forces, as depicted in Figure 7. The simulation also captures the influence of the thin shale layer located between elevations z = 27.0 and 27.3 m, which functions as a significant hydraulic barrier within the vadose zone. The lower permeability of the shale impedes vertical transmission, resulting in a localized increase in water saturation immediately above this unit. Additionally, the shale unit causes the ponded water at the alluvium-santdstone interface directly benath the infiltration pond to spread laterally across the width of the domain.

From the right panels of Figure 8, it is evident that within the saturated zone—between elevations z = 0 and 6 m—both the porous medium and the fracture network remain fully water-saturated. Immediately above this interval, within the capillary fringe, water saturation in the fractures drops rapidly toward residual values. This sharp transition reflects the strong capillary forces and rapid drainage response in the fracture apertures once pressures fall below hydrostatic conditions. This demonstrates the impact of the low capillary pressures within the fracture apertures of the DFN relative to that of the adjacent matrix, as shown in Figure 7. Fractures with water saturations above residual near the shale unit represent zones where water drainage was restricted due to the shale's low permeability and strong capillary entry pressures. The shale behaves as a hydraulic barrier, reducing vertical transmissivity within the rock matrix and thereby increasing water saturation in the shale and the overlying materials to near unity and even exhibit perched water table conditions. Consequently, fractures immediately above the shale experience saturations above residual, thus becoming dominant features for water flow. Contrastingly, the fractures within the unsaturated areas of the vadose zone serve as conduits for active gas phase flow, while the matrix blocks serve as the medium for water infiltration. Finally, the very low ambient recharge rate is sufficient to maintain elevated water saturations within the Chatsworth Formation matrix at the CTL-III area within the entire vadose zone thickness prior to the initiation of BVE.

Alluvium sediments immediately above the bedrock, between elevations z = 34 to 40m, exhibit their highest water saturation where they contact the bedrock, as well as within fine-grained

pond liner sediments. Both the water and gas phases are above residual saturation and mobile within the alluvium. Note that the alluvium is unconsolidated and hence does not contain fractures.

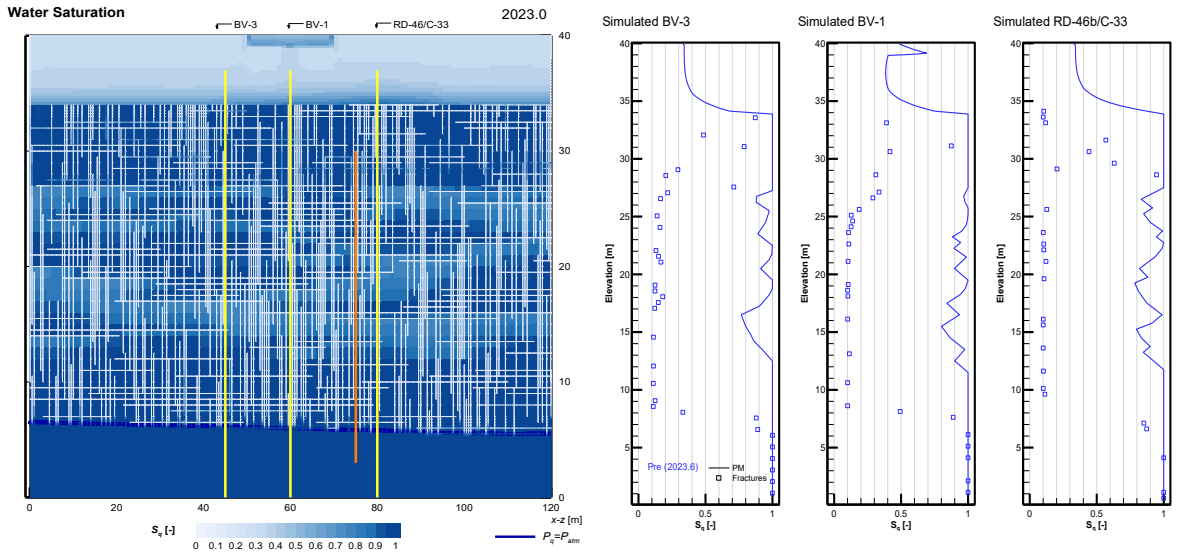


Figure 8 : Simulated water saturation distribution across the numerical domain. The 2-D cross-section (left) illustrates the contrast between the porous matrix and the discrete fracture network and spatial variability in saturation in the vadose zone. The three vertical profile plots (right) compare the saturation of the Porous Medium against the Fracture network as a function of depth.

Figure 9 presents field-measured versus simulated water content profiles as denoted by the yellow profile locations at x = 45 m, 60 m, and 80 m on Figure 8. Measured water content values show significant variability with depth due to variations in matrix water saturation, porosity, mineralogy and hence specific gravity of the sandstone solid phase, and consequently the bulk density of any given core sample interval used to assess moisture content. Simulated water content values were computed by post-processing CFBioF as described in Section 3.4.1.

Specifically, simulated water saturation values along the profile locations were converted to water content using lower-, median- and upper-bounds of field-measured porosity values from core samples that were also used to measure water content directly. The resulting simulated water content profiles using the median porosity closely replicate field values while the upper- and lower-bounds capture the variability along each profile.

Note that the simulated profiles are smoother than the measured data because the numerical model represents the bedrock as a continuum and does not incorporate sample-scale heterogeneity along each core. Remaining discrepancies between simulated and measured values likely reflect fracture distributions, -small-scale porosity variations, and textural differences not explicitly parameterized in the model. Nonetheless, the close agreement in overall magnitude and general depth structure demonstrates that the porosity–saturation framework used in the model provides a reasonable representation of the antecedent moisture distribution within the bedrock vadose zone.

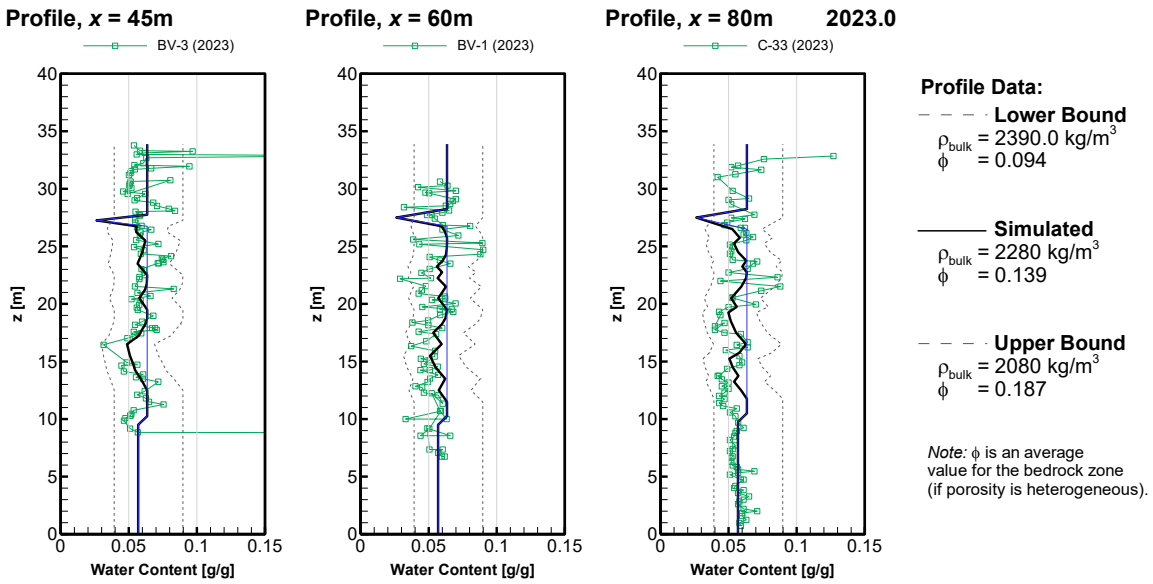


Figure 9 : Integrated comparison of CFBioF-simulated water content profiles with 2023 field measurements (Jacobs, 2025) at three horizontal positions.

4.1.2 Comparison of Simulated to Measured TCE Distribution

Figures Figure 10 and Figure 11 illustrate the evolution of TCE in a three-phase system, where contamination exists as both DNAPL (trapped in the pond) and as solute or vapour in the aqueous and gas phases, respectively.

The early-time temporal evolution of TCE is shown in Figure 10, where saturation index (SI) values greater than zero represent NAPL saturation (S_n) and values below zero are orders of magnitudes below solubility concentration, $\log_{10}(C/C_{\text{solubility}})$. From 1959 to 1970, the simulations show the redistribution and gradual dissolution and disappearance of DNAPL in the pond. During initial discharge of TCE in the ponded infiltration water from 1959 to 1960, TCE DNAPL appears but is localized to the central part of the infiltration pond and does not breach the pond liner into the alluvium beneath. This TCE DNAPL then continues to dissolve into the infiltrating pond water with disappearance of the DNAPL source zone by 1970. The resulting TCE aqueous phase plume spreads laterally and vertically due to advective transport in the infiltrating water by both gravity drainage as well as capillary forces between the matrix and fracture in the bedrock vadose zone, as well as by phase partitioning between the ambient gas and aqueous phases and aqueous/gas phase diffusive transport within the vadose zone. Advective transport of TCE in the gas is minimal as the gas phase redistributes itself to accommodate the infiltrating ponded water. During ponded water infiltration from 1959 to 1972 during epoch 2, a perched water table appeared beneath the infiltration pond at the alluvium-bedrock interface. This perched water table acted to spread the TCE aqueous phase plume laterally across the domain within the alluvium and was key to providing a match between the simulated and measured TCE bedrock profiles shown below. Note that by end of epoch 3 in 2023, this perched water table had infiltrated into the bedrock as shown on Figure 8.

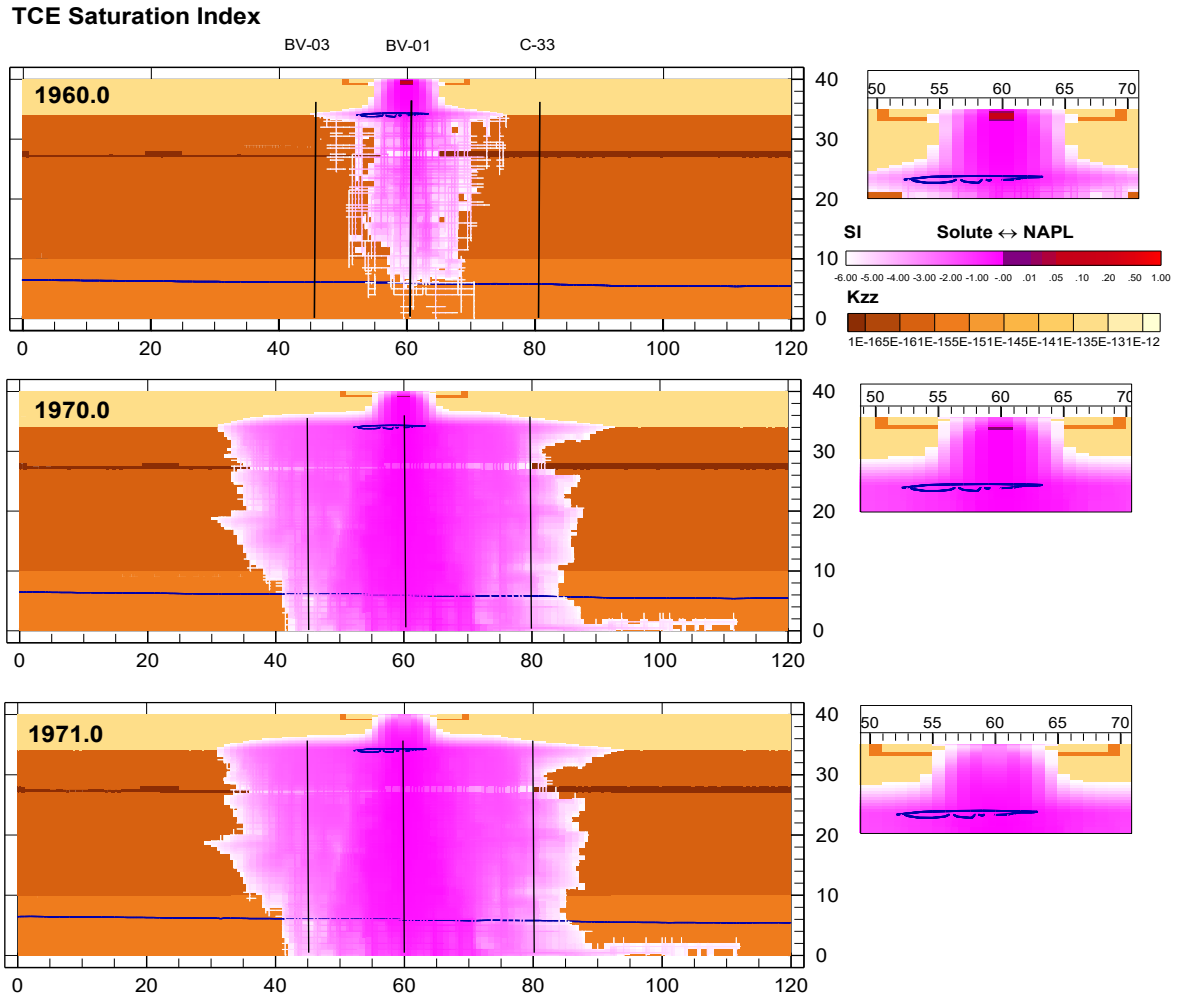


Figure 10 : Numerical simulation of TCE saturation index (SI) evolution for the years 1960, 1970, and 1971, showing DNAPL and its subsequent disappearance driven by dissolution processes. Note: the zoomed insets show DNAPL presence at 1960 (mobile, dark red) through 1970 (residual, plum), and solute only in 1971 (magenta). The perched water table at the alluvium-bedrock interface is outlined in blue.

Over time, TCE partitions from immobile DNAPL at residual-saturation into the more mobile aqueous and gas phases. In these forms, it can move through fractures and slowly diffuse into the surrounding rock matrix, contributing to long-term persistence. Overall, this reflects typical DNAPL behaviour in fractured bedrock, where dissolution and diffusion reduce the source zone while spreading contamination into more mobile and less accessible areas.

Figure 11 presents the simulated spatial distribution of TCE concentrations at three representative times: 1960, 1972, and 2023, which correspond to the end of TCE injection during epoch 2, the end of ponded water infiltration during epoch 2, and the end of epoch 3, respectively, as described in Section 3.3.1. This sequence of images illustrates the simulated historical flow and transport of TCE in the subsurface by depicting the aqueous and gas phase distribution of TCE in the vadose zone, which then serve to ground-truth the model results

through comparison with available field observations. The results illustrate the progressive expansion and redistribution of the vapour and dissolved TCE plume under the influence of infiltration, subsurface heterogeneity, fracture-matrix interactions, sorption onto the solid phase, and first-order decay as a representation of abiotic and biotic degradation (Yu et al., 2020). Parameters used in the CFBioF numerical model to simulate these TCE concentrations are itemized in Table 1 and described throughout Section 3.4.2.

With respect to the solute plume only shown in Figure 11, in 1960, the TCE distribution was characterized by the gravity-driven descent of dissolved TCE through the pond liner and into the alluvium, and fractured bedrock. Migration of the TCE progresses via advective flux in the infiltrating water which exhibits preferential flow paths along fractures. The water saturation within these fractures is sufficiently above residual to allow water to be mobile. Significantly, matrix diffusion (the transfer of dissolved mass from fractures into the low-permeability matrix) is in its early stages with high concentration gradients between the fractures and rock matrix; the contaminant remains largely "accessible" within transmissive zones, as the sequestration into the stagnant matrix that leads to long-term back-diffusion has not yet matured (Pankow & Cherry, 1996). Note that matrix diffusion is driven by both aqueous and gas phase diffusion of TCE within the fractures and matrix within the vadose zone. The relative importance of gaseous versus aqueous diffusion as a mass transport mechanism is primarily a function of water/gas phase saturation and TCE diffusion coefficient, which both proportionally scale the TCE diffusive flux. The gas-phase diffusion coefficient is typically several orders of magnitude greater than aqueous-phase diffusion coefficient. Consequently, gas diffusive flux dominates mass transfer in drier regions or periods, enabling rapid contaminant redistribution. Conversely, high water content (e.g., during active infiltration) chokes air-filled pores, shifting the dominant mechanism to the aqueous diffusive flux. This balance varies both spatially with moisture profiles and temporally as saturation levels fluctuate (Millington & Quirk, 1961); equilibrium partitioning, however, keeps the solute and vapour plume fronts equal.

By 1972 (the point when focused pond recharge stops), the simulated plume in the unsaturated zone has exhibited substantial growth in both lateral and vertical directions. Once TCE reaches the saturated zone, groundwater flow becomes the dominant driver of plume migration, resulting in pronounced downgradient spreading below the water table. The plume widens considerably, indicating the diffusive exchange between high-permeability features and the adjacent porous matrix. This behaviour is characteristic of dual-domain transport systems, where fractures or features act as fast conduits while the matrix progressively accumulates dissolved contaminant mass. (Parker et al., 1994). As a result, TCE concentrations become more spatially distributed, with lower but more extensive concentration levels extending beyond the initial source region. Note that the early time occurrence of TCE DNAPL in the alluvium has been completely dissolved by the infiltrating pondwater.

Finally, in 2023, the TCE plume has reached its maximum spatial extent, exhibiting a broad, laterally continuous distribution of low-to-moderate concentrations and a substantially diminished high-concentration core. The simulation indicates the absence of DNAPL; TCE

exists entirely in the dissolved phase in the saturated zone and as dissolved and vapor phases in the vadose zone. Since the initial release, several key processes have shaped the plume: advective flushing and recharge. Continued steady recharge has driven flushing, mobilizing dissolved TCE from the vadose zone into the saturated zone and sustaining advective transport along fractures (Pankow & Cherry, 1996). This process effectively depletes the source zone over time as clean water infiltrates the system. Diffusion in both the aqueous and gas phases has promoted lateral spreading, smoothing of concentration gradients and extending the plume laterally beyond high-permeability pathways (Pankow & Cherry, 1996). In the vadose zone, vapor-phase diffusion can significantly accelerate the expansion of the footprint compared to aqueous transport alone. Matrix diffusion has sequestered dissolved mass in low-permeability domains, a process that significantly impacts plume longevity in fractured media (B. L. Parker et al., 1994). While this initially reduces peak concentrations in the fractures, subsequent back-diffusion contributes to an ongoing, long-term release that sustains the plume even after the primary source is depleted. Concurrently, degradation processes, including reductive dechlorination (Freedman, 1989) in the saturated zone, have reduced overall TCE mass and attenuated peak concentrations. The effectiveness of these natural degradation processes is critical for the transition of the plume toward a stable or receding state (Wiedemeier et al., 1998), and are quantified in a subsequent section. The plume geometry in 2023 reflects the cumulative effects of advective flushing, diffusive redistribution, matrix storage, and natural attenuation.

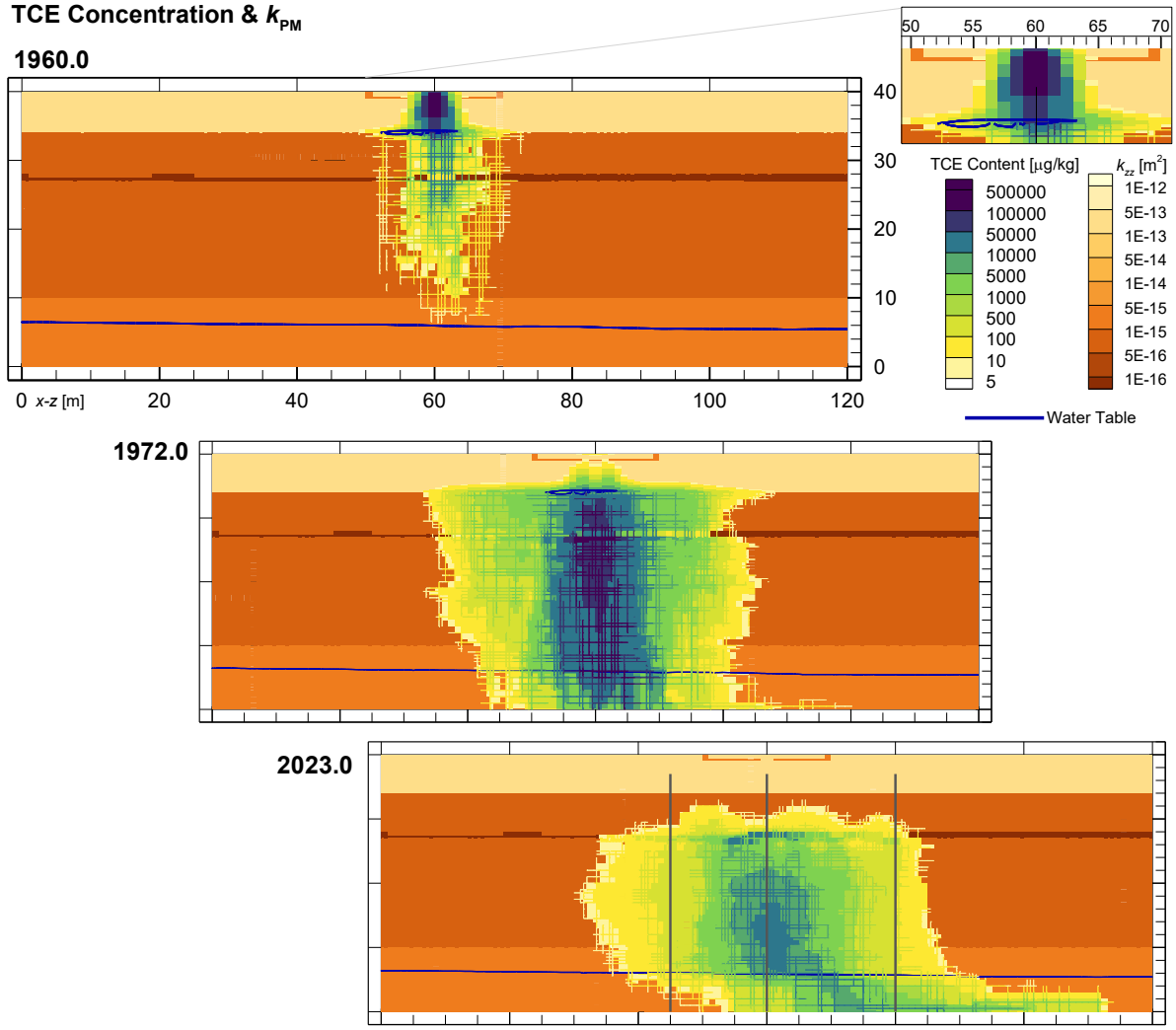


Figure 11 : Spatial visualizations of the simulated Total Equivalent TCE (all phases) mass fraction within the bulk wet rock (TCE Content) at three pre-BVE time snapshots, superimposed on the intrinsic vertical permeability field of the rock matrix (k_{zz}): 1960, marking the end of TCE DNAPL injection in the pond; 1972, marking the cessation of enhanced pond infiltration; and 2023, immediately prior to BVE implementation. Vertical markers on the 2023 panel denote the locations of the vertical profiles corresponding to BV-3, BV-1, and C-33.

Figure 12 presents a comparison between the simulated total TCE mass fraction (black line) and the core-derived TCE mass fractions measured at three borehole locations (BV-3, BV-1, and RD-46B/C33) plotted at their corresponding lateral positions of x = 45 m, x = 60 m, and x = 80 m. The measured data are shown as green markers for 2023 samples and brown markers for the historical 1997 samples (Jacobs, 2025). To facilitate direct comparison with core measurements, the simulation output is plotted as an equivalent, all-phases TCE mass fraction of rock, meaning that both aqueous-phase TCE as well as sorbed-phase TCE are included in the total mass fraction calculation.

Alongside the simulated profile, two additional curves are provided: an upper bound (dashed line) and a lower bound (dotted line). These are not alternative simulation scenarios; rather, they represent post-processing transformations of the simulated aqueous phase TCE concentration using site-observed variability in porosity and bulk density to illustrate the sensitivity of mass fraction estimates to local matrix properties. While this approach introduces a conceptual inconsistency when considering plume-scale mass balance, it is methodologically consistent with how rock-core mass fraction measurements are traditionally interpreted, particularly when core samples lack direct co-located measurements of ρ_{bulk}, ϕ, and f_{oc}. In such cases, analysts must make explicit or implicit assumptions about representative matrix properties to back calculate in situ sorbed mass from laboratory extraction data. Therefore, the adopted approach maintains internal consistency at the individual sampling point, which is the appropriate scale for comparing core-derived values with model predictions.

To calculate the upper and lower bounds at each point where core-derived TCE mass fractions were obtained, the simulated aqueous concentration field is reevaluated using upper and lower bound values of bulk density ρ_{bulk} and matrix porosity ϕ as itemized in Table 1, as:

$$R_{\text{matrix}} = 1 + \frac{\rho_{\text{bulk(dry)}}\, K_d}{\phi} = 1 + \frac{\rho_{\text{bulk(dry)}} (f_{OC} K_{OC})}{\phi} \tag{4.1}$$

Based on the site characterized organic carbon fraction and partition coefficient. The resulting retardation factor determines the ratio of sorbed to dissolved TCE phases and directly influences the total mass fraction derived from the simulated concentrations.

Across the three profiles, the simulated mass fraction (black line) generally falls within the scatter of modern (2023) measurements and provides a reasonable envelope for the historical (1997) values as well. The green 2023 data tend to show greater scatter than the brown 1997 values, consistent with the broader vertical variability observed in recent core data at BV-3 and BV-1. The simulation captures the first-order vertical structure of TCE mass distribution. Differences between simulation and measured values at individual depths reflect a combination of (i) true small-scale heterogeneity in porosity and organic carbon content that are not reflected in the block-wise homogenous PM layers and (ii) methodologically unavoidable uncertainties in translating laboratory extraction results to in situ mass fractions.

Across the three profiles, the lower bound and simulated lines are extremely close to one another, to the degree that they cannot be visually distinguished from one another. In the plotted profiles, a direct consequence of the similarity between the slightly varied porosity density pair and the Lower Bound pair. Thus, the apparent overlap is expected and not indicative of numerical or conceptual error. In contrast, the Upper Bound curve departs from both the Simulated profiles. This separation arises from the higher bulk density, lower porosity, ϕ, and consequently larger retardation factor, R_{matrix}, used in the Upper Bound scenario.

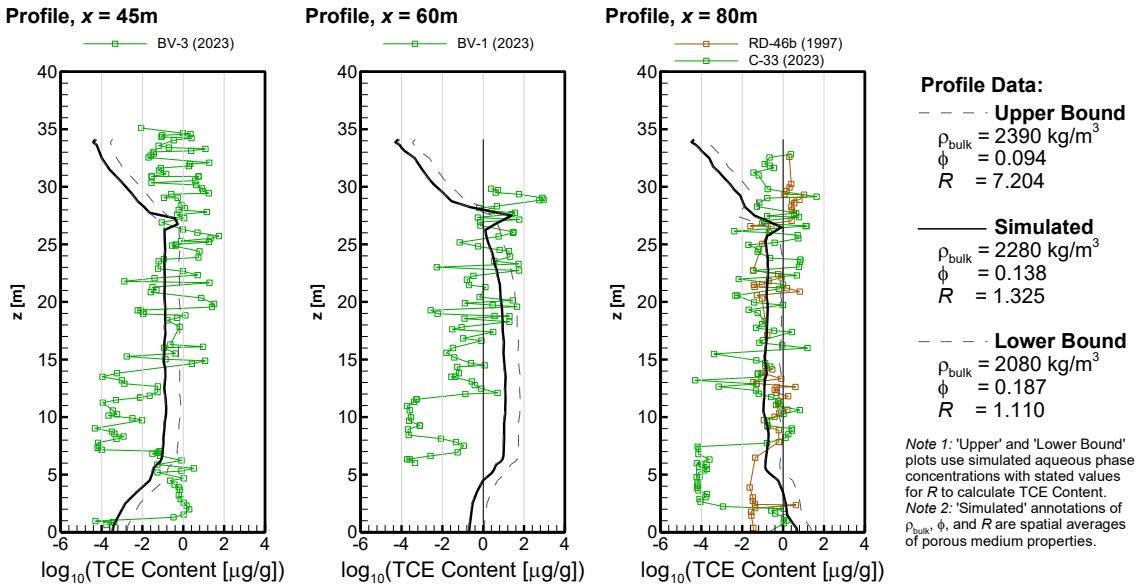


Figure 12 : Simulation results expressed as equivalent, all-phases TCE mass fraction in rock, compared with core-derived TCE mass fraction measurements at three core locations (BV-3, BV-1, RD-46b/C-33, replotted from (Jacobs, 2025, Appendix A) and corresponding positions in the simulation domain. Lower and Upper bound mass fraction estimates are computed by applying site-observed porosity and bulk density variability point-wise to the simulated aqueous TCE concentrations.

Both the simulated and core-derived TCE mass fractions depicted in Figure 12 indicate the no DNAPL present at the three core locations. Moreover, as shown in Figure 10, the 3-phase period of the simulation shows DNAPL only existing within the infiltration pond and adjacent alluvium during TCE loading and shortly thereafter from 1959 to 1961. This simulated DNAPL never reached the bedrock and dissolved into the infiltrating ponded water by the end of epoch 2 in 1972. This agreement between modelled and observed conditions implies validation of the conceptual and numerical models. It suggests that any historical DNAPL release has been depleted or transformed into dissolved-phase contamination within the infiltrating groundwater over time, and that the current groundwater plume behaviour is governed by slow aqueous-phase diffusive mass transport from low-permeability near-fully-water-saturated matrix zones rather than ongoing DNAPL dissolution. Such long-term persistence of dissolved plumes controlled by matrix diffusion has been widely documented in fractured and heterogeneous subsurface environments (B. L. Parker et al., 2008).

Figure 13 depicts a two-dimensional contour map of the field-derived TCE distribution between boreholes BV-3, BV-1 and RD-46B/C-33 (Weaver, 2026, personal communication). These contours originate from a 40 m-wide, unit-thickness section (cut out from the 3-D geologic block model of TCE mass fraction interpolated from rock core measurements) centred around boreholes BV-3, BV-1, and C-33, representing the high-resolution mid-section of the retention-pond area in 2023. Notably, these three cored holes span a transect that effectively bounds the presumed input location (the pond). Defining this specific area in the field sets the stage for the analogous 40m cross-section utilized in the model domain, allowing for a direct comparison between interpolated rock core measurements and simulated TCE mass

distributions below the source area. Recall that Figure 11 represents the analogous simulated TCE distribution, derived from a two-dimensional simulation on a computation domain that is 120 m wide with unit thickness. The model uses block-wise homogeneous properties in a flat-lying configuration, which averages out lateral heterogeneity and fracture-controlled small-scale variability. Because the field transect corresponds to only the central portion of the simulation domain, any comparison should focus on the general structure of the source zone rather than a direct one-to-one spatial match.

Both the field-derived (Figure 13) and simulated TCE distributions (Figure 11) show comparable plume morphology, with a high mass fraction in the vadose zone that is hydraulically connected to elevated concentrations in the saturated zone. The simulation further demonstrates sustained mass discharge to groundwater, indicating an integrated vadose–saturated system rather than vertical confinement of the source.

Because the numerical model is 2-D, flow paths are constrained to lie strictly within the plane of the cross-section. This forces the development of laterally continuous zones of elevated concentration that appear connected in 2-D, whereas in a fully three-dimensional system, flow paths and high concentration zones could bypass the 2-D slice entirely and would not necessarily appear in the cut-out cross-section. The combination of the bedrock–alluvium interface and the imposed pond recharge rate further promote a laterally wide dissolved phase flow path in the 2-D representation, producing a broader region of high concentration.

In contrast, the field-derived 3-D interpolation captures abrupt changes in concentration over short vertical distances—often more than an order of magnitude between adjacent samples—reflecting the strong influence of anisotropy in the fracture network and/or heterogeneous matrix properties. The simulated results do not show this level of small-scale variability, as the 2-D model does not capture the dip angle or true connectivity of the fracture network and it averages heterogeneous matrix properties within larger grid cells. This difference is expected and does not indicate a model error; rather, it reflects the fundamental contrast between high-resolution field measurements and the simplifications inherent in a 2-D simulation.

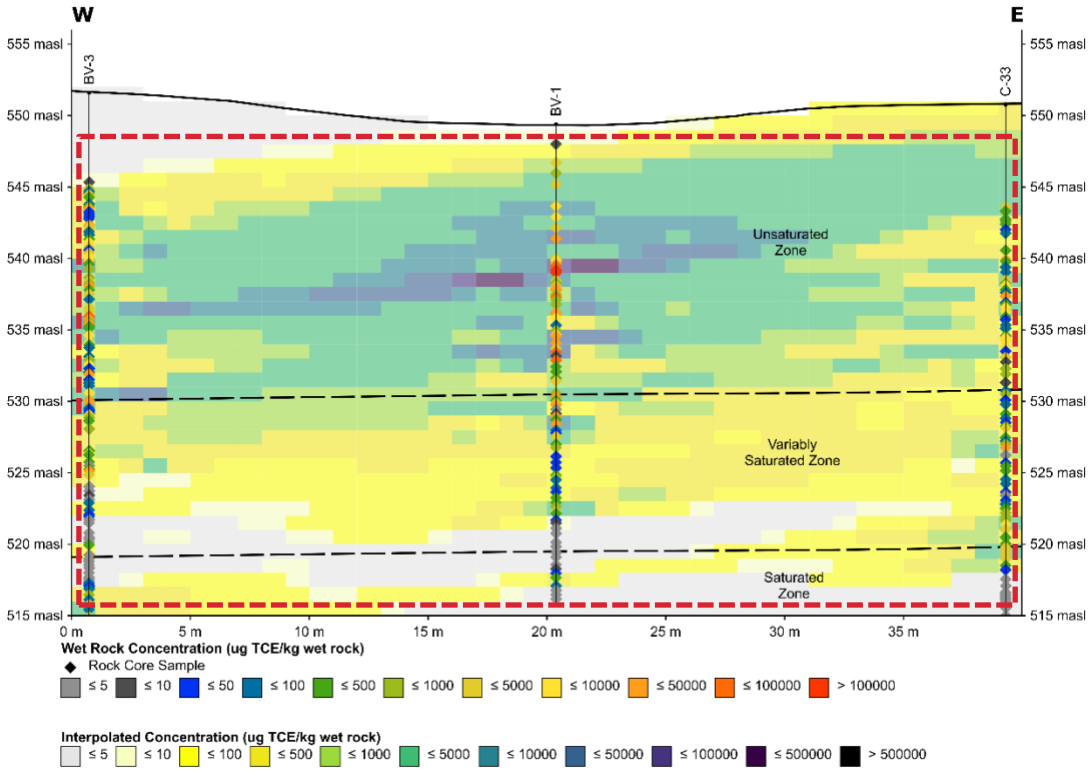


Figure 13 : Spatial distribution of total equivalent TCE within the rock matrix (colour fill) as interpolated from rock core measurements (dots in well traces) into a 3-D geologic block model (Weaver, 2026, personal communication). 'Variably Saturated' describes the changing water table elevation during the Pilot Test, from the drilling of holes to the monitoring of the BVE operations, rather than rock matrix pore water conditions. The red dashed box indicates the approximate extent of mass summation appearing in other figures, for spatial reference.

Table 2 compares the total equivalent TCE mass estimated from a 40 m-wide, unit-thickness slice of the 3-D geologic block model with the mass simulated in an analogous 40 m-wide cutout from 2-D model at pre- and post-BVE times. The 3-D geological model cutout estimates a total mass of 7.19 kg, with the majority of TCE residing in the unsaturated bedrock vadose zone (6.85 kg), and comparatively minor contributions from the variably saturated (0.25 kg) and fully saturated bedrock (0.09 kg) intervals. No soil samples were included for the alluvial unit in the 3-D estimate. In the 2-D simulation, the pre-BVE total mass (7.21 kg) closely matches the 3-D-derived value, indicating good mass consistency between conceptualizations despite differences in dimensionality and model width. Following BVE simulation, the total mass decreases to 6.60 kg, reflecting a measurable but modest reduction in vadose-zone mass, primarily within the bedrock vadose interval. The strong agreement between the 3-D-derived and 2-D pre-BVE mass estimates supports the representativeness of the 2-D model geometry and parameterization for evaluating remedial performance, while the post-BVE results demonstrate that residual mass remains predominantly within the vadose bedrock system.

Table 2 : Total equivalent TCE mass from a 40 m-wide, unit-thickness cut-out from the 3-D geologic block model (Weaver, 2026, personal communication) versus mass in 40 m-wide cutout of the 120 m-wide 2-D simulation.

Zone	3-D Geologic Model Cutout		2-D Simulation Cutout		
	Zone	Total TCE Mass [kg]	Zone	PRE BVE Total TCE Mass [kg]	POST BVE Total TCE Mass [kg]
Alluvium	*(No soil samples included.)*		Vadose-Alluvium *40 m × 6 m z=34-40 m*	2×10^{-5}	6×10^{-6}
Bedrock Vadose Zone	Unsaturated *40 m × 20 m ~530-550 masl*	6.85	Vadose-Bedrock *40 m × 26 m z=8-34 m*	5.56	5.04
	Variably Saturated *40 m × 10 m ~520-530 masl*	0.25			
Bedrock-Saturated Zone	*Saturated 40 m × 5 m ~515-520 masl*	0.09	Saturated *40 m × 8 m z=0-8 m*	1.65	1.56
	Total	**7.19**		**7.21**	**6.60**

4.2 BVE Pilot Study

4.2.1 Comparison of Simulated to Measured Vacuum Response

The Pilot Test was conducted by applying a 50 kPa vacuum pressure (5 m of water equivalent) as measured at the blower applying the vacuum to the BVE well. Note that atmospheric gas pressure is estimated to be 101.3 kPa. Figure 14a depicts the measured vacuum response in the bedrock vadose zone. A vacuum response of 1 m of water equivalent was observed at a distance of 5 to 10 m radially from the BVE well, decreasing to 0.1 m at a distance of 25 m radially. The response is laterally distributed but vertically constrained, reflecting anisotropy of the fracture network with bedding parallel fractures consistent with the site's dipping. Gas leaks in the piping that deliver the vacuum created at the blower to the well screen are assumed to account for the 40 kPa difference between what was applied and what was measured in the subsurface over a 5-meter distance from the well screen.

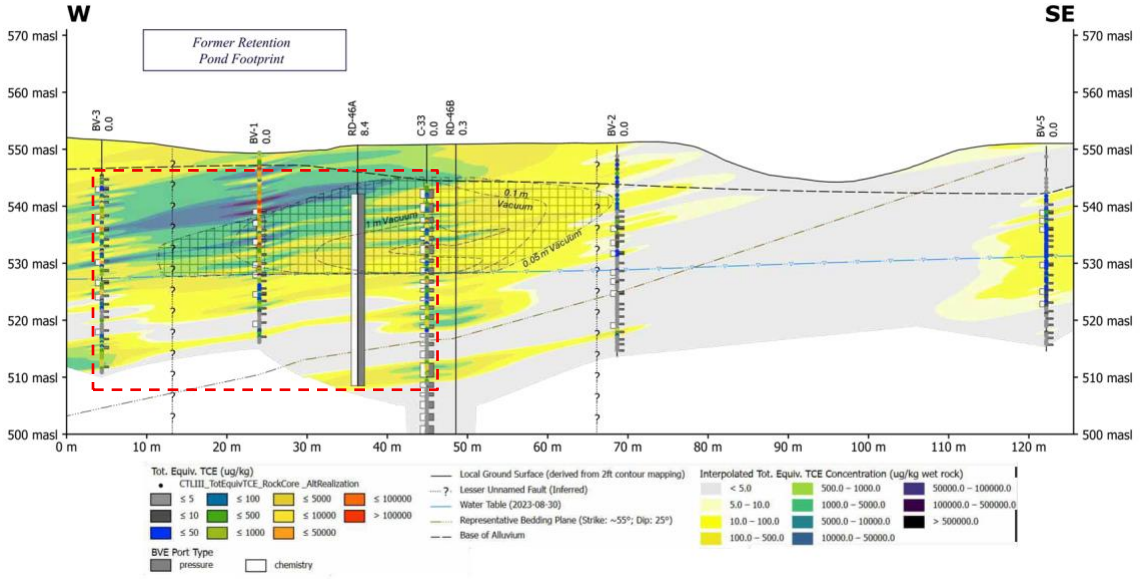
Figure 14b depicts the simulated vacuum response used to replicate the measured vacuum near the BVE well, with a simulated vacuum pressure of 10 kPa (1 m of water equivalent) at the well screen. Given that the simulated reference atmospheric pressure was 100 kPa, the pressure of the vacuum well was therefore 90 kPa. The modelled pressure response is strongly influenced by the vertical intrinsic permeability (k_{zz}), which governs vertical pressure dissipation and the efficiency of vacuum transmission across lithostratigraphic boundaries. The reduced k_{zz} assigned to the shale layer limits vertical pressure transfer through the shale matrix and promotes partial vertical decoupling between lithostratigraphic units. However, the gas-response pattern does not represent disconnected regions. Gas-filled fractures provide the primary pneumatic pathway linking the atmospheric boundary at the top of the domain to the

BVE well, enabling pressure propagation around the low-permeability high-water-content shale and maintaining hydraulic continuity between the upper and mid-depth zones.

The asymmetric response observed in the alluvium is controlled by a laterally extensive horizontal fracture (at x = 60–95 m and z = 34 m), which governs the dominant flow path from the top atmospheric boundary toward the extraction well. The 0.1 and 0.05 iso-vacuum contours extend laterally to the sides of the domain and align with vertical fracture features that were incorporated to facilitate pneumatic connection between the mid-depth zone and the atmosphere.

Because the model employs continuous and idealized k_{zz} distributions and simplified fracture representations, vertical pressure transfer is more spatially uniform than in the heterogeneous field setting. As a result, a slightly stronger applied vacuum (90 kPa absolute pressure at the well) is required in the simulation to reproduce the observed 1 m vacuum response in the field.

a)



b)

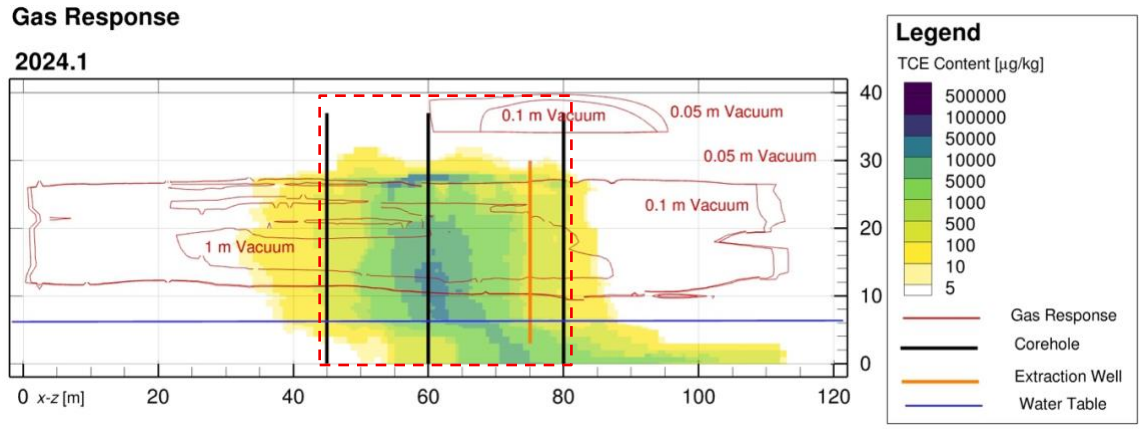


Figure 14 : a) Measured gas pressure distribution within the fractured bedrock domain during active Bedrock Vapour Extraction. (Appendix A – MG360 – SSFL CTL-III BVE Pilot Test Report 2025). b) Simulated gas-phase vacuum pressures (iso-lines) distribution within the fractured bedrock domain during active BVE (reported as a fractional year). The red dashed box in both panels indicates the approximate spatial extent of mass summation from the 3D interpolated geologic block model.

Figure 15 presents the simulated vertical profiles of the fracture and matrix gas-phase pressures (P_g) as well as velocity magnitude ($|v_g|$) at BV-3 at x=45m, BV-1 at x=60m, and C-33 at x=80m within the model domain for pre-BVE conditions (2023.0), near the end of extraction (2024.1), and immediately following shutdown (2024.2). The simulated fracture and matrix water saturation along the same BV-3, BV-1, and C-33 profiles are shown in Figure 16.

The pre-BVE fracture gas phase pressure $P_{g,}$ within the vadose zone is uniformly near atmospheric, increasing slightly with depth due to gas phase density. In contrast, matrix gas

phase pressure is near atmospheric when the matrix has sufficient gas phase saturation for a mobile gas phase. However, in regions where the matrix is fully water saturated and the gas phase is immobile with negligible $|v_g|$, the gas pressure of the gas phase increases above atmospheric pressure in response to the hydrostatic water phase pressure. This is evident in the interval between elevations 28 and 34m and again below 13 m.

During BVE (2024.1), the gas phase pressure drawdown is transmitted through both fractures and matrix, but the velocity response clearly demonstrates fracture-dominated flow. Gas velocities within fractures are several orders of magnitude greater than those in the matrix, confirming that the fracture network controls advection of the gas extraction induced by the vacuum imposed by the BVE well, whereas the matrix primarily responds through pressure diffusion with minimal contribution to bulk gas transport. Closer inspection of fracture-specific responses reveals a more complex and depth-dependent behaviour, particularly near and below the water table or within the saturated portion of the domain. In contrast, at intermediate depths, the fracture response is comparatively muted, with little measurable change during or after BVE. This vertical variability underscores the importance of fracture architecture, connectivity, and local transmissivity contrasts in governing system response. The vertical water saturation profiles from BV-3, BV-1, and C-33 (Figure 16) indicate that BVE produced a modest increase in matrix water saturation below the shale layer (z=25-27m).

The post-BVE (2024.2) profiles show a system undergoing partial pressure recovery following the cessation of the applied vacuum and active gas phase extraction. Gas velocity magnitudes decrease substantially from their peak BVE levels but remain higher than pre-BVE values, reflecting persistent advective transport dominated by fractures, which continue to transmit gas-phase flow even after extraction has stopped due to the slow redistribution of water saturations returning to ambient conditions. Overall, BVE leaves the fundamental water saturation architecture of the fractured bedrock system largely intact, with only transient and depth-specific fracture responses superimposed on a matrix-dominated, capillary-controlled framework.

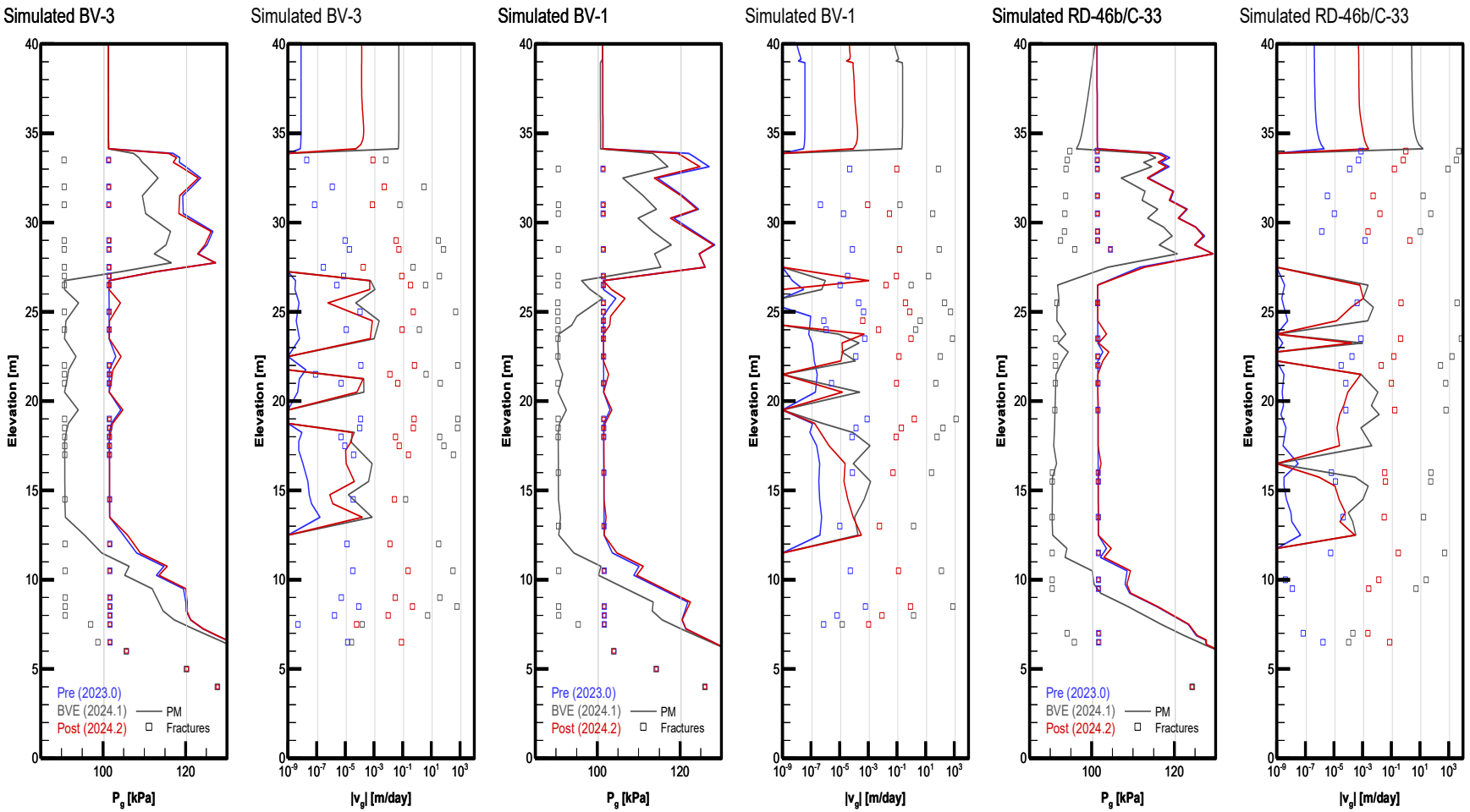


Figure 15 : Simulated profiles of gas phase pressure (P_g) and velocity magnitude ($|v_g|$) for locations BV-3, BV-1, and C-33 at times before BVE (2023.0), near the end of BVE (2024.1) and immediately following BVE (2024.2)

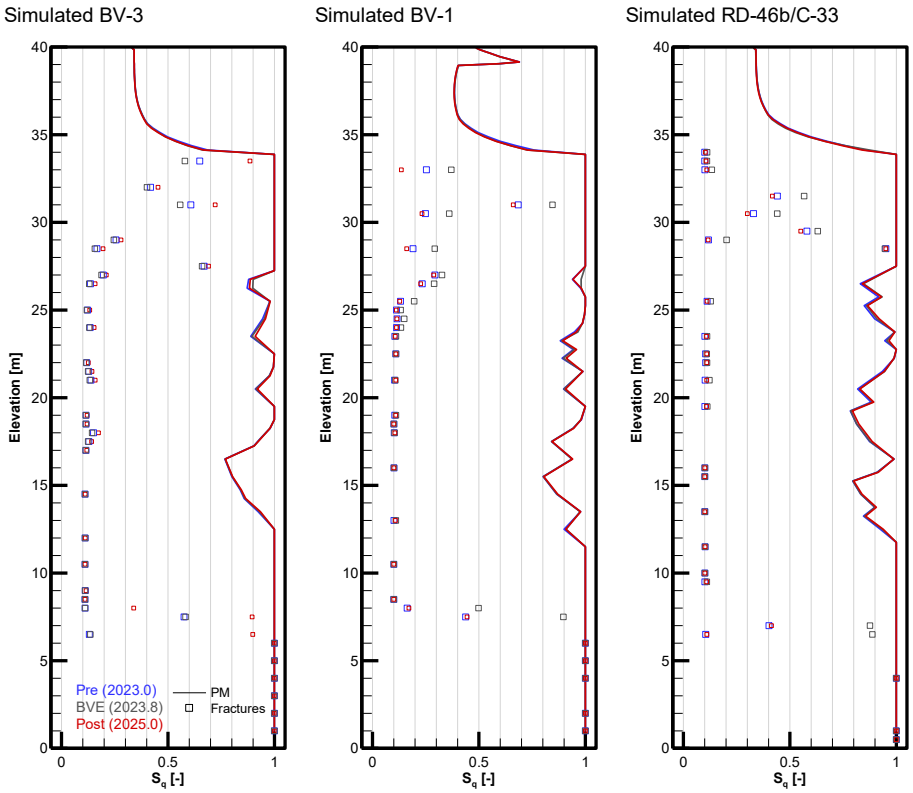


Figure 16 : Vertical water saturation profiles before, during (near end) and after BVE (+10 months) in the simulated borehole locations BV-3, BV-1, and C-33.

4.2.2 Simulated TCE Vapour Response

Figure 17 presents the simulated TCE gas vapour concentration profiles at BV-3, BV-1, and C-33 for pre-BVE conditions (2023.0), near the end of BVE (2023.8), and following BVE shutdown (2025) and into the future (2050).

The simulated pre-BVE (2023) fracture and matrix concentrations are identical at all boreholes, indicating local equilibrium within the vadose zone due to long-term advective-diffusive mass transport between fractures and the adjacent matrix of solute- and vapour-form TCE. Note that TCE concentrations decrease in regions where the water saturation approaches unity both surrounding the shale layer as well as beneath the water table. This would imply that gas phase diffusion within the vadose zone is primary mechanism for distributing across the domain. Additionally, first-order decay of TCE within the matrix blocks removes TCE faster than water infiltration as well as aqueous phase diffusion can replenish it.

During BVE (2023.8), the TCE vapour concentrations in the fractures decreased by several orders of magnitude relative to pre-BVE conditions. In contrast, matrix concentrations remained relatively invariant from their pre-BVE state. This is a consequence of advective flushing of the fractures with the clean atmospheric air being drawn towards the BVE well screen. The elevated water saturation within the bedrock matrix further reduces the gas phase mobility advective and diffusive vapour transport within the matrix. Despite the appearance of

strong concentration gradients between the matrix and adjacent fractures, diffusive mass loss from the matrix (dissolved and vapour phases) is limited, as indicated in the next time snapshot.

The post-BVE (2025) profiles indicate that TCE vapour concentrations within the fractures quicky re-equilibrate with adjacent matrix values to near pre-BVE levels. This rebound indicates that the bedrock matrix acted as a reservoir and persistent source of TCE to fractures. Matrix concentrations themselves remained nearly unchanged from pre-BVE to post-2025, confirming that the 6-month extraction period was insufficient to significantly perturb the large TCE mass reservoir in the bedrock matrix.

The long-term post-BVE simulation (2050) reveals a different behavior. Over the subsequent decades, both fractures and matrix exhibit gradual decreases in TCE concentrations, including within the shale-bounded interval around 27 m elevation. This long-term decline reflects continued first-order decay combined with downward flushing toward the water table (where rates are quantified and discussed in a subsequent section). The more rapid reduction in upper-domain concentrations indicates that mass removal is primarily driven by downward vertical migration via “clean” infiltrating water. Nevertheless, even by 2050, substantial residual concentrations persist in the bedrock matrix and in deeper intervals below the water table, where BVE influence was limited, and mass transfer remains aqueous diffusion controlled.

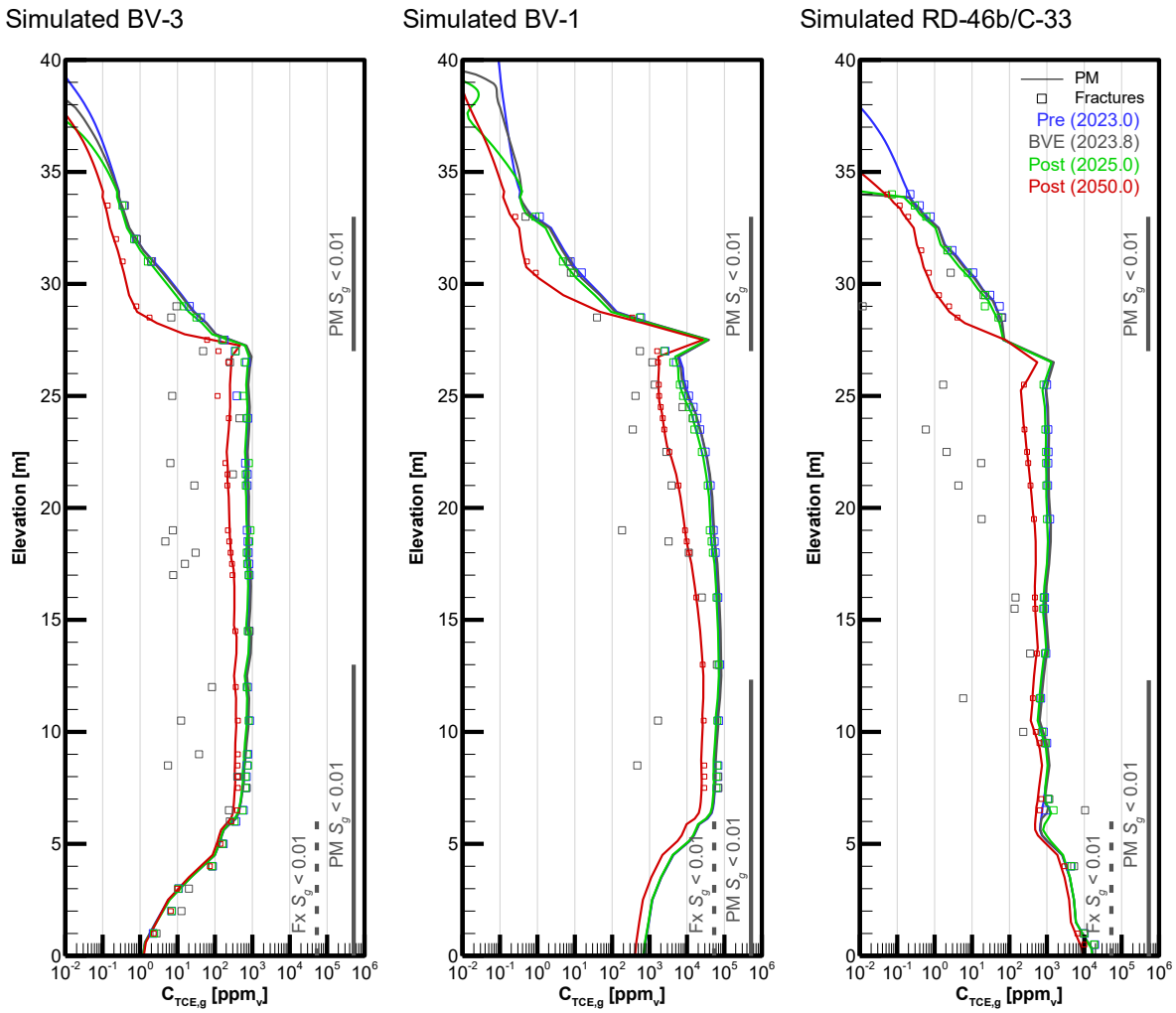


Figure 17 : Vertical TCE concentrations in the gas phase before, during (near end) and at near and future times after BVE in the analogous simulated borehole locations BV-3, BV-1, and C-33.

4.2.3 Simulated Water Infiltration Response

Figure 18 illustrates the simulated infiltration rate of water through the fracture and matrix continua across four horizontal planes that transverse the entire domain. The first plane is located at an elevation of z = 27 m, which is immediately below the shale layer, while the second and third planes are located at elevations of z = 25 m and 15 m, which are in the vadose zone, and finally, the fourth is located at z = 8 m, which is immediately above the water table. Simulated discharge values are shown over the period from early 2023 through early 2025, encompassing pre-BVE, active BVE (mid-2023 to early 2024), and post-BVE conditions.

Immediately below the shale layer in the vadose zone, where the matrix water saturation is near unity, the fractures conduct the majority of the infiltrating water over the entire simulation period. In contrast, for flux planes at z = 25 m, 15 m and 8 m, where the matrix is partially saturated with water, the matrix conducts the majority of the infiltrating water. This is because

the capillary pressure difference between the fracture and adjacent matrix ensures the majority of the infiltrating water remains in the matrix as it drains downwards. However, sufficient water does remain mobile within the fractures (S_q values just exceeding $S_{q,residual}$) to create the fast preferential flow paths for TCE mass transport seen in Figure 11.

Note that during BVE, the flux plane at z = 27 m exhibits a large increase in water infiltration while the flux plane at = 8 m remains relatively constant, aside from the perturbation when the BVE vacuum was immediately applied. The perched saturated zone in the alluvium and sandstone bedrock above the shale layer transfers water to the variably saturated zone below in response to BVE vacuum, resulting in an increase in water infiltration at z = 27 m. This redistribution of water remains in the vadose zone and manifests itself as an increase in water saturation within the matrix and fractures of up to 0.05. However, this redistribution of water within the vadose zone does not result in a commensurate change in water infiltration to the water table. In contrast, the vacuum applied by the BVE does cause a local rise in the water table, albeit with that rise remaining below the z = 8 m flux plane.

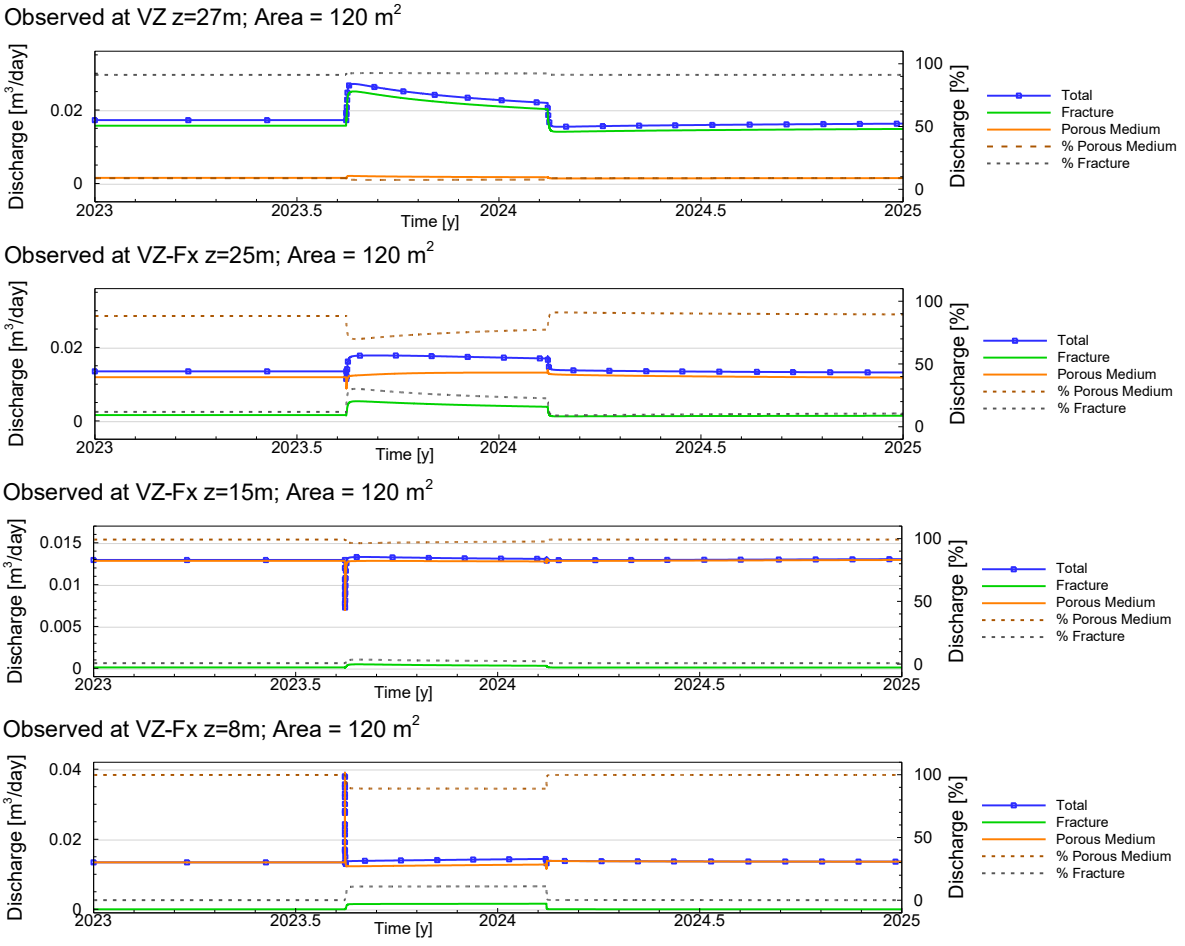


Figure 18 : Simulation results showing porous medium versus fracture aqueous phase discharge (as solid lines) and discharge proportion (as dashed lines) over horizontal planes at various elevations in the vadose zone (elevations as indicated).

4.3 Impact of BVE on Vadose Zone TCE Mass Removal and Groundwater Flux Reduction

Figure 19a shows the simulated cumulative TCE mass which estimate residence in the whole domain (pond, vadose-zone and saturated zone) from 1960 to 2060. It indicates that the simulated TCE mass residence in the vadose zone is characterized by multi-decadal persistence. Initially, TCE mass accumulated rapidly in the vadose zone during epoch 2 as TCE was loaded into the infiltration pond concurrent with enhanced infiltration at the pond. TCE then primarily accumulated within the vadose zone bedrock below (see 'Resident, VZ BR'). This behaviour reflects the long residence time of chlorinated solvents in the vadose zone as observed in porous media (Brusseau et al., 2013; B. L. Parker et al., 2008), where mass transfer limitations, diffusion into lower-permeability domains, and slow desorption processes govern long-term attenuation. Discharge to the water table represents the second long-term mass-loss pathway. The cumulative discharge curve (see 'Discharge cumulative') shows that a substantial portion of the original vadose-zone mass has been transferred to groundwater over time. This indicates that groundwater loading has historically been controlled by vertical mass flux from the unsaturated zone. The long-term decline in resident mass is therefore primarily a function of first-order decay (i.e., degradation) and sustained discharge to the saturated zone, which has a prominent early-time effect during pond-focused infiltration.

Figure 19b focuses specifically on the simulated BVE operational period during which the total TCE mass lost is approximately 0.52 kg from vapour extraction (BVE), discharge to the water table, and degradation combined. The 'BVE Cumulative' plot quantifies the mass directly attributable to vapour extraction during the active remediation phase, which is 0.15 kg. The BVE operation corresponds to an overall extraction efficiency of approximately 3% of the available resident mass at the start of the event. This indicates that under the applied vacuum conditions, the BVE system recovered only a limited fraction of the available mass. However, this modest efficiency reflects the distribution of TCE between advectively accessible fracture domains and storage within the low-permeability rock matrix. Vapour extraction primarily increases advective gas velocities within fractures and other permeable pathways that fall within the zone of pressure influence of the extraction system. In contrast, a substantial fraction of the contaminant mass resides within the bedrock matrix, where gas velocities are very low and vapour transport is governed by diffusion, limited gas saturation and relative permeability, and sorption processes. As a result, contaminant mass must first transfer from the matrix into the fracture network before it can be captured by the extraction system, which constrains the achievable removal rate during BVE operation.

Figure 19c shows that degradation rates are lower than early advective discharge fluxes (due to strong infiltration-driven flushing and steep concentration gradients immediately following TCE loading), and degradation operates continuously throughout the simulation period. Over multi-decadal timescales, this steady contribution becomes increasingly important in controlling residual mass.

Figure 19d indicates when the mass-loss rates are compared over the BVE operational period, BVE represents the dominant short-term removal pathway; however, degradation continues to

contribute steadily and discharge to the water table remains an active component of the system mass balance. Consequently, while the system response confirms that engineered extraction enhances short-term mass removal, the magnitude of removal relative to the remaining mass indicates that long-term attenuation processes continue to govern the broader evolution of the vadose-zone source. Figure 19d also indicates that the simulated discharge to the water table increases when BVE is active. This demonstrates that vacuum extraction perturbs the subsurface aqueous phase flow system and enhances overall TCE mass flux to groundwater, resulting in a temporary rise in downward mass transfer toward the groundwater system. Such responses have been observed in vapour extraction systems where pressure-induced phase redistribution alters contaminant flux pathways (Johnson et al., 1990).

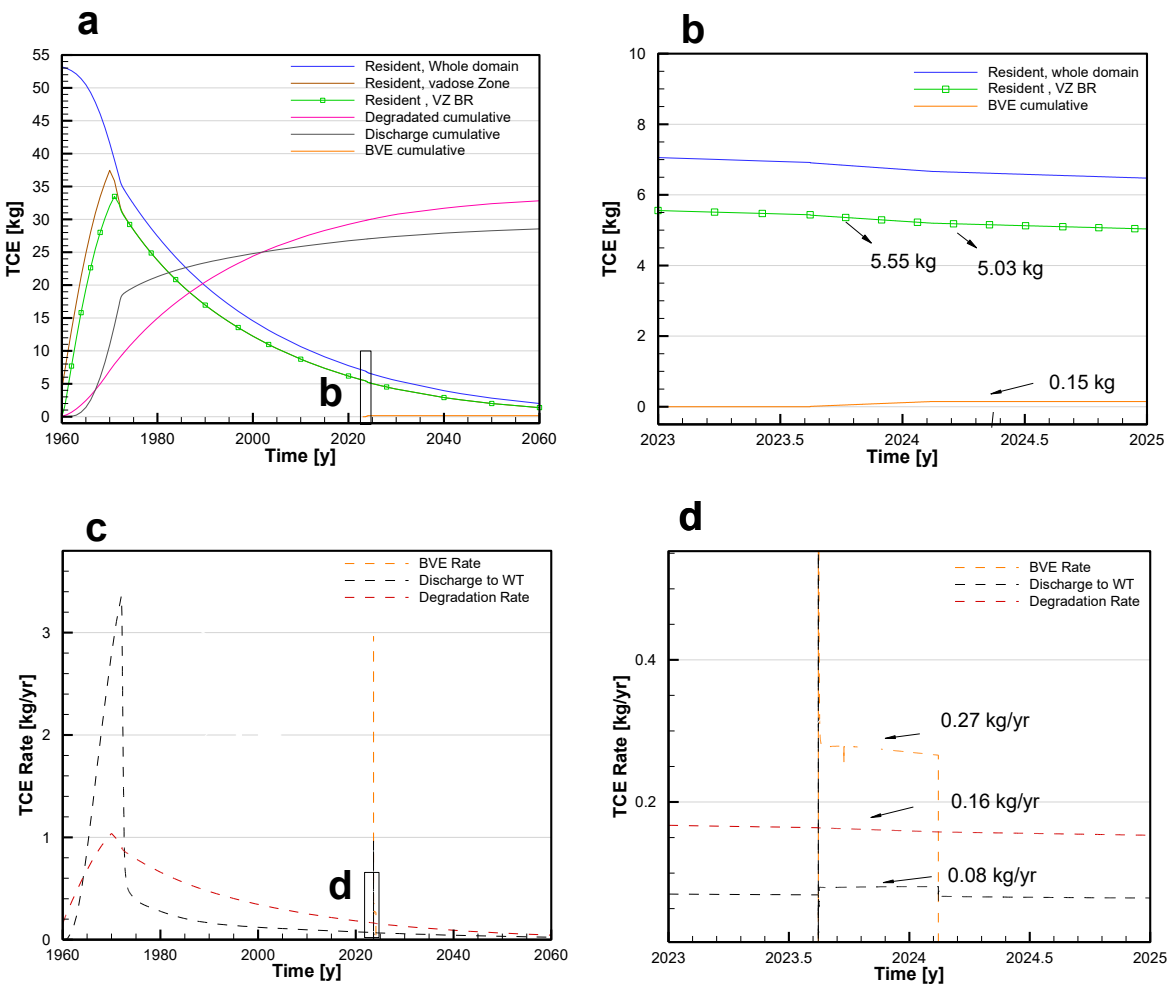


Figure 19 : Simulated evolution of TCE mass and TCE rates in the 2-D simulation domain. (a) Long-term view of resident mass, cumulative losses due to discharge to the water table and decay from 1960 to 2060. (b) Short-term view of mass from 2023 to 2025, focused on the time surrounding the BVE operational period. (c) Long-term mass-loss rates due to BVE, discharge to the water table and decay. (d) Short-term view of mass-loss rates surrounding the BVE operational period.

In the field, the BVE Pilot Test's total TCE mass removed was evaluated using discrete TO-15 laboratory vapour analyses (taken bi-weekly at RD-46A (Jacobs, 2025)). These datasets were analyzed separately and through statistical modelling to provide multiple lines of evidence for estimating overall removal (Jacobs, 2025). Because only 13 TO-15 samples were collected during the 6-month duration of the test, regression-based methods were employed to better characterize concentration trends over time. Figure 20shows an estimated TCE removal of about 524 lbs when these concentration measurements are combined with the average air flow rates (Jacobs, 2025). Note that this estimate assumes steady conditions between sampling intervals and does not account for short-term fluctuations in flow or concentration. In the field, the BVE Pilot Test's total TCE mass removed was evaluated using discrete TO-15 laboratory vapour analyses (taken bi-weekly at RD-46A (Jacobs, 2025)). These datasets were analyzed separately and through statistical modelling to provide multiple lines of evidence for estimating overall removal (Jacobs, 2025). Because only 13 TO-15 samples were collected during the 6-month duration of the test, regression-based methods were employed to better characterize concentration trends over time. Figure 20 shows an estimated TCE removal of about 524 lbs when these concentration measurements are combined with the average air flow rates . Note that this estimate assumes steady conditions between sampling intervals and does not account for short-term fluctuations in flow or concentration.

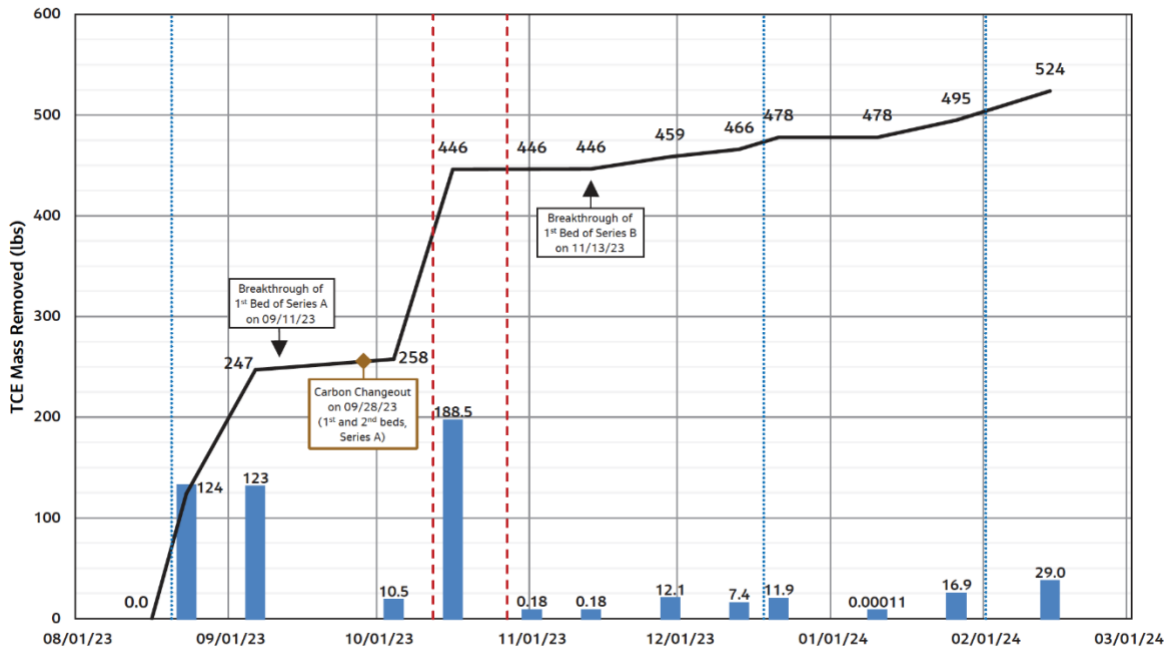


Figure 20 : Cumulative TCE mass removed during BVE operations, calculated using interval-averaged influent concentrations and flow rates. Short-term variability in system flow and temporal declines in influent concentration is not reflected in this estimate. Reprinted Figure 11-8 from (Jacobs, 2025).

A comparison between the 2-D numerical simulation results (Figure 19) and the field BVE pilot system performance (Figure 20) reveals a substantial difference in cumulative mass removal over the six-month operational period. The simulation predicts approximately 0.15 kg

of cumulative TCE removal under 90 kPa applied vacuum at the well screen, whereas the field system reports 524 lbs (~238 kg) removed under 50 kPa vacuum at the blower, over the same duration. We reiterate that the measured vacuum in the subsurface during the pilot study was nearly identical to that which was simulated.

Multiple hydrogeologic and methodological factors explain why the divergence in mass removal is rational and scientifically defensible, with these factors detailed below.

The dimensionality of the systems is fundamentally different. The numerical model represents a 2-D cross-sectional domain, whereas the field pilot system operates in a fully 3-D heterogeneous subsurface environment. In three-dimensional systems, airflow converges radially toward extraction wells, producing a significantly larger radius of influence and volumetric treatment zone. By contrast, a 2-D model constrains lateral airflow and limits the effective capture volume. Because contaminant mass removal in BVE systems is directly proportional to treated soil volume and airflow convergence geometry, it is physically expected that a 3-D field system would extract substantially more mass than a 2-D representation operating over the same time frame. Therefore, the greater cumulative removal shown in Figure 20 relative to Figure 19b is consistent with geometric scaling effects.

Methodological consideration involves the use of average flow rates in mass calculations. Vacuum extraction systems commonly experience transient airflow conditions due to operational adjustments, barometric pressure changes, and subsurface permeability variability. If averaged flow rates are applied across extended periods without high-frequency validation, cumulative mass removal may be biased (EPA, 1991). Given the limited number of discrete laboratory samples and reliance on statistical smoothing, the reported cumulative removal in Figure 20should therefore be interpreted as an estimate subject to uncertainty rather than a continuously measured value.

Accordingly, the lower cumulative mass removal predicted by the 2-D simulation is consistent with geometric scaling constraints and domain limitations, while the field estimate represents a full 3-D operational system subject to measurement and statistical uncertainty. Therefore, the difference reflects differences in physical representation and data estimation methodology rather than an inconsistency in hydrogeologic principles.

Chapter 5
Conclusions

This study utilized the CompFlow BioF (CFBioF) to develop a two-dimensional (2-D) numerical modelling framework to simulate trichloroethylene (TCE) transport in the aqueous and gaseous phases within a fractured-porous sedimentary rock vadose zone. In particular, by utilizing the conceptual model and field-derived data of the CTL-III operations area at the Santa Susana Field Laboratory (SSFL), the performance of a bedrock vapour extraction (BVE) pilot test within the heterogeneous Chatsworth formation sandstone was evaluated (see Jacobs, 2025). Consequently, validation of the model involved replicating key hydrogeological characteristics of the vadose zone as observed by detailed subsurface measurements, including discrete fracture observations, core sample analysis, geophysical measurements, multilevel well observations. The intent was to demonstrate that the CFBioF modelling framework can capture the dominant processes governing contaminant transport in the system and effectively represent relevant field observations, and therefore be used to assess the efficacy of BVE for fractured-porous formations.

The hydrologic behaviour of the CTL-III site area was evaluated by using the model to simulate field-observed water content and flow in the matrix and fractures for conditions before, during, and after BVE operation. The results demonstrate a clear depth-dependent partitioning of discharge that is controlled by lithostratigraphy, relative permeability contrasts, and pneumatic/hydraulic connectivity. Fracture-dominated water flow is most pronounced at the shale layer, where the low permeability of the water-saturated matrix significantly restricts downward infiltration. In contrast, matrix-dominated water flow occurs below the shale layer at intermediate depths and near the water table, while fractures play only a limited role given that they remain at near residual water saturation. BVE operation results in a temporary increase in fracture discharge at all depths; however, water discharge quickly reverted to pre-BVE. matrix-dominated discharge conditions once the system ceased operation.

The fate and transport of TCE at the CTL-III site area, as well as the effectiveness of BVE as a remediation technology, was evaluated by using the model to simulate; antecedent TCE mass fraction profiles in core samples, the total observed mass distribution of TCE in the vadose zone, TCE mass removal by the BVE well, gas pressure response due to the vacuum pressure imposed by the BVE well, its radius of influence, and long-term mass loading of TCE to the saturated zone. Comparison with field measurements shows some discrepancies between the simulated and observed total TCE mass removed by the BVE well. However, the assessment of observed mass removal was limited by lack of sufficient sampling data as well as the geometric difference between the 2-D model and real-world 3-D field conditions. Key sources of divergence include geometric scaling effects that constrain airflow convergence and capture volume in 2-D, idealized fracture connectivity, and the averaging of heterogeneous matrix properties that control gas flow and contaminant availability. In addition, the model assumes simplified, steady extraction and diffusion-controlled fracture–matrix mass transfer, whereas the field system reflects 3-D transient airflow, barometric influences, and localized fracture-dominated release. Despite these differences, both the simulation and field pilot test show a

consistent, stratigraphically controlled gas pressure response, with laterally extensive but vertically limited vacuum propagation. The model reproduced a similar ~1 m water head vacuum response, consistent with field observations, although it predicts a larger radius of influence. This difference primarily reflects dimensionality: the 3-D field system allows radial flow and pressure dissipation in all directions, while the 2-D representation constrains flow to a plane, promoting lateral pressure transmission and overestimating lateral extent. Overall, the discrepancies are physically defensible and highlight the need for future 3-D, higher-resolution modelling to improve quantitative agreement to field conditions.

The effectiveness of BVE in this fractured porous rock vadose-zone system is governed by the strong contrast between advective mass transport of TCE in the gas phase within the fracture network, and much more limited advective and diffusive mass transport of TCE within the aqueous and gas phases from within low-permeability/porosity and predominately water-saturated rock matrix towards the fracture-matrix interface and into the fracture network. As a result, BVE induces a pronounced concentration gradient between fractures and matrix, while matrix-to-fracture mass transfer remains rate-limiting, constraining the overall BVE mass removal efficiency. Consequently, while BVE is effective at removing the advectively accessible vapour-phase TCE mass within fractures, it does not substantially deplete the larger TCE mass reservoir within the matrix. This leads to rapid post-BVE rebound of vapour concentrations as the system pressure gradients re-equilibrate, highlighting that BVE performance is ultimately controlled by the coupling between fast gas-phase fracture flow and slow matrix aqueous-phase diffusion. Therefore, in fractured rock settings such as CTL-III, BVE acts primarily as a short-term mass removal mechanism, while long-term plume persistence and attenuation remain governed by matrix storage and diffusion-driven back-transfer processes, and biodegradation.

References

Amirtharaj, E. S., Ioannidis, M. A., Parker, B., & Tsakiroglou, C. D. (2011). Statistical Synthesis of Imaging and Porosimetry Data for the Characterization of Microstructure and Transport Properties of Sandstones. *Transport in Porous Media*, *86*(1), 135–154. https://link.springer.com/article/10.1007/s11242-010-9612-x

Bairos, K., Quinn, P., Pehme, P., & Parker, B. L. (2023). Enumerating hydraulically active fractures using multiple, high-resolution datasets to inform plume transport in a sandstone aquifer. *Journal of Hydrology*, *619*, 129362. https://doi.org/10.1016/j.jhydrol.2023.129362

Bear, J., Tsang, C. F., & Marsily, G. de. (1993). *Flow and contaminant transport in fractured rocks*. Academic Press, San Diego, CA (United States). https://www.osti.gov/biblio/37095

Berre, I., Doster, F., & Keilegavlen, E. (2019). Flow in Fractured Porous Media: A Review of Conceptual Models and Discretization Approaches. *Transport in Porous Media*, *130*(1), 215–236. https://link.springer.com/article/10.1007/s11242-018-1171-6

Brusseau, M. L., Carroll, K. C., Truex, M. J., & Becker, D. J. (2013). *Characterization and Remediation of Chlorinated Volatile Organic Contaminants in the Vadose Zone*. https://doi.org/10.2136/vzj2012.0137

CH2MHILL. (2008). *Group 5 – Central Portion of Areas III and IV RCRA Facility Investigation Report Santa Susana Field Laboratory, Ventura County, California*.

Chapman, S., & Parker, B. (2005). Plume persistence due to aquitard back diffusion following dense nonaqueous phase liquid source removal or isolation. *Water Resources Research*, *41*. https://doi.org/10.1029/2005WR004224

EPA. (1991). *Soil Vapor Extraction Technology Reference*.

EPA. (2001). *Methods for Collection, Storage and Manipulation of Sediments for Chemical and Toxicological Analyses: Technical Manual* ((EPA 823-B-01-002)). U.S. Environmental Protection Agency.

EPA. (2011). *Toxicological Review of Trichloroethylene* (Summary Information on the Integrated Risk Information System (IRIS) EPA/635/R-09/011F). U.S. Environmental Protection Agency.

Forsyth, P. A. (1994). *Three-dimensional modelling of steam flush for DNAPL site remediation*. https://onlinelibrary.wiley.com/doi/abs/10.1002/fld.1650191202

Freedman, D. L. (1989). Biological reductive dechlorination of tetrachloroethylene and trichloroethylene to ethylene under methanogenic conditions. *Applied and Environmental Microbiology*, *55*(9), 2144–2151. https://doi.org/10.1128/aem.55.9.2144-2151.1989

Freeze, R. A., & Cherry, J. A. (1979). *Groundwater*. Prentice-Hall.

Ho, C. K., & Webb, S. W. (Eds.). (2006). *Gas Transport in Porous Media*. Springer Netherlands. https://doi.org/10.1007/1-4020-3962-X

Hurley, J. C. (2003). *Rock Core Investigation of DNAPL Penetration and Persistence in Fractured Sandstone*. University of Waterloo.

Hutzler, N. J., Murphy, E. E., & Gierke, J. C. (1989). *State of Technology Review: Soil Vapor Extraction Systems*. United States Environmental Protection Agency.

ITRC. (2017). *Characterization and remediation of fractured rock*.

Jacobs. (2025). *Bedrock Vapor Extraction Pilot Study Report, Component Test Laboratory III, Santa Susana Field Laboratory, Ventura County, California* (250530142821_a577cb35; Submitted to Boeing Inc., p. 3990). Jacobs Inc.

Jacobs, & Morwick G360 Groundwater Research Institute. (2022). *Bedrock Vapor Extraction Pilot Study Work Plan, Component Test Laboratory III, Santa Susana Field Laboratory, Ventura County, California*. https://www.dtsc-ssfl.com/files/lib_feasibilitystudy/feasibilitystudywork/69715_Boeing_SSFL_BVE_WorkPlan_091622.pdf

Jung, Y., Pau, G. S. H., Finsterle, S., & Pollyea, R. M. (2017). TOUGH3: A new efficient version of the TOUGH suite of multiphase flow and transport simulators. *Computers & Geosciences, TOUGH Symposium 2015: Recent Enhancements to the TOUGH Family of Codes and Coupled Flow and Geomechanics Processes Modeling*, *108*, 2–7. https://doi.org/10.1016/j.cageo.2016.09.009

Keller, A. A., & Chen, M. (2003). Effect of spreading coefficient on three-phase relative permeability of nonaqueous phase liquids. *Water Resources Research*, *39*(10). https://doi.org/10.1029/2003WR002071

Kueper, B. H., & McWhorter, D. (1991). *The Behavior of Dense, Nonaqueous Phase Liquids in Fractured Clay and Rock*. https://ngwa.onlinelibrary.wiley.com/doi/10.1111/j.1745-6584.1991.tb00563.x

Lipson, D. S., Kueper, B. H., & Gefell, M. J. (2005). Matrix diffusion-derived plume attenuation in fractured bedrock. *Ground Water*, *43*(1), 30–39. https://doi.org/10.1111/j.1745-6584.2005.tb02283.x

Mackay, D. M., Wilson, R. D., Brown, M. J., Ball, W. P., Xia, G., & Durfee, D. P. (2000). A controlled field evaluation of continuous vs. pulsed pump-and-treat remediation of a VOC-contaminated aquifer: Site characterization, experimental setup, and overview of results. *Journal of Contaminant Hydrology*, *41*(1), 81–131. https://doi.org/10.1016/S0169-7722(99)00065-0

Manna, F., Kennel, J., Weaver, Laura, Pierce, A., Pehme, P., Walton, K., & Parker, B. (2025). *Groundwater Investigations and Bedrock Vapour Extraction Pilot Test in the CTL-III Area at Santa Susana Field Laboratory*. Morwick G360 Groundwater Research Institute, University of Guelph, Ontario, Canada.

Mendoza, C. A. (1992). *Capillary pressure and relative transmissivity relationships describing two-phase flow through rough-walled fractures in geologic materials* [Doctoral Thesis]. University of Waterloo.

Millington, R. J., & Quirk, J. P. (1961). *Permeability of Porous Solids.* (57), 1200–1207. https://doi.org/10.1039/tf9615701200

Montgomery-Watson. (2000). *Conceptual Site Model Movement of TCE in the Chatsworth Formation* [TECHNICAL MEMORANDUM].

MWH. (2004). *Santa Susana Field Laboratory Report of Results phase 1 of Northeast Investigation area groundwater characterization* (Volume I of III). MWH.

MWH. (2020). *Final RCRA Facility Investigation Data Summary and Findings Reports, Boeing RFI Subarea 1A Central, Santa Susana Field Laboratory, Ventura County, California*. https://www.dtsc-ssfl.com/files/lib_rcra_soils/boeingsubarea1acntrl/Final_RFI_Rpts/69157_2020.01.10_04_HVN_DSFR_20200108.pdf

NASA. (2015). *Results from Bravo Bedrock Vapor Extraction Treatability Study*.

National Research Council. (1994). *Alternatives for Ground Water Cleanup.* The National Academies Press. https://doi.org/10.17226/2311

National Research Council. (2005). *Contaminants in the Subsurface: Source Zone Assessment and Remediation* (p. 11146). National Academies Press. https://doi.org/10.17226/11146

Neretnieks, I. (1980). Diffusion in the rock matrix: An important factor in radionuclide retardation? *Journal of Geophysical Research: Solid Earth*, *85*(B8), 4379–4397. https://doi.org/10.1029/JB085iB08p04379

Pankow, J. F., & Cherry, J. A. (1996). *Dense Chlorinated Solvents and Other DNAPLs in Groundwater: History, Behavior, and Remediation*.

Parker, B., Cherry, J., Manna, F., Pierce, A., Abbey, D., Martin, P., & Andrachek, R. (2020). *Groundwater Flow System SCM at SSFL: Advanced Insights from the 3-D Mountain Scale Numerical Flow Model* (p. 46) [Technical Memorandum].

Parker, B. L., Chapman, S. W., & Guilbeault, M. A. (2008). Plume persistence caused by back diffusion from thin clay layers in a sand aquifer following TCE source-zone hydraulic isolation. *Journal of Contaminant Hydrology*, *102*(1–2), 86–104. https://doi.org/10.1016/j.jconhyd.2008.07.003

Parker, B. L., Cherry, J. A., & Chapman, S. W. (2012). Discrete fracture network approach for studying contamination in fractured rock. *AQUA Mundi*, *3*(2), 101–116.

Parker, B. L., Gillham, R. W., & Cherry, J. A. (1994). Diffusive Disappearance of Immiscible-Phase Organic Liquids in Fractured Geologic Media. *Ground Water*, *32*, 805–820. https://doi.org/10.1111/j.1745-6584.1994.tb00922.x

Pedersen, T. A., & Curtis, J. T. (1991). *Soil Vapor Extraction Technology*.

SSFL Groundwater Advisory Panel. (2009). *Site Conceptual Model for the Migration and Fate of Contaminants in Groundwater at the Santa Susana Field Laboratory, Simi, California: Overview and 20 Site Conceptual Model Elements DRAFT* (Prepared for The Boeing Company, National Aeronautics and Space Administration, and United States Department of Energy, p. Volumes 1-4). University of Guelph.

Stantec. (2021). *Boeing Final Groundwater RCRA Facility Investigation Report. Santa Susana Field Laboratory, Ventura County, California.* (Stantec PN: 185704114). Stantec Consulting Services Inc.

Sterling, S. N., Parker, B., Cherry, J., Williams, J. H., Lane, J. W., & Haeni, F. P. (2005). *Vertical cross contamination of trichloroethylene in a borehole in fractured sandstone*. https://doi.org/10.1111/j.1745-6584.2005.0087.x

Sterling, S. N., & Parker, B. L. (1999). *Rock core sampling and analysis for volatile organic concentrations and hydraulic parameters in boreholes RD-35B and RD-46B at the Santa*

Susana Field Laboratory, California [Report]. Department of Earth Sciences, University of Waterloo.

Sudicky, E. A., & McLaren, R. G. (1992). The Laplace Transform Galerkin Technique for large-scale simulation of mass transport in discretely fractured porous formations. *Water Resources Research*, *28*(2), 499–514. https://doi.org/10.1029/91WR02560

Unger, A. J. A., Sudicky, E. A., & Forsyth, P. A. (1995). *Mechanisms Controlling Vacuum Extraction Coupled With Air Sparging for Remediation of Heterogeneous Formations Contaminated by Dense Nonaqueous Phase Liquids*. https://agupubs.onlinelibrary.wiley.com/doi/abs/10.1029/95WR00172

USACE. (2002). *Soil Vapor Extraction and Bioventing:* Defense Technical Information Center. https://doi.org/10.21236/ADA329943

Walton, K. M. (2013). *On Modeling Three-Phase Flow in Discretely Fractured Porous Rock* [PhD Thesis, Department of Earth Science]. University of Waterloo.

Walton, K. M., Unger, A. J. A., Ioannidis, M. A., & Parker, B. L. (2019). Benchmarking NAPL Redirection and Matrix Entry at Fracture Intersections Below the Water Table. *Water Resources Research*, *55*(4), 2672–2689. https://doi.org/10.1029/2018WR023435

Walton, K., Parker, B., Motakefghomi, K., & Unger, A. J. A. (2025). *Insights in TCE Mass Discharge to Groundwater using Multi-Phase DFM Simulations; Santa Susana Field Laboratory, Ventura County, California*.

Weaver, L., Manna, F., Walton, K., Kennel, J., & Parker, B. (2024). *Three-dimensional Trichloroethene Impact Mapping and Mass Estimation in the CTL-III Bedrock Vapour Extraction Study Area; Santa Susana Field Laboratory, Ventura County, California*. Morwick G360 Institute for Groundwater Research.

Wiedemeier, T. H., Swanson, M. A., Moutoux, D. E., Gordon, E. K., Wilson, J. T., Wilson, B. H., Kampbell, D. H., Haas, P. E., Miller, R. N., Hansen, J. E., Chapelle, F. H., & Carolina, S. (1998). *Technical Protocol for Evaluating Natural Attenuation of Chlorinated Solvents in Ground Water*.

Wilson, J. T. (1996). Remediation apparatus and method for organic contamination in soil and groundwater. *U.S. Patent*.

Yoon, H., Kim, J. H., Liljestrand, H. M., & Khim, J. (2002). Effect of water content on transient nonequilibrium NAPL - Gas mass transfer during soil vapor extraction. *Journal of Contaminant Hydrology*, *54*(1–2), 1–18. https://doi.org/10.1016/S0169-7722(01)00164-4

Yu, R., Murdoch, L. C., Falta, R. W., Andrachek, R. G., Pierce, A., Parker, B. L., Cherry, J. A., & Freedman, D. L. (2020). Chlorinated Ethene Degradation Rate Coefficients Simulated with Intact Sandstone Core Microcosms. *Environmental Science & Technology*, *54*(24), 15829–15839. (WOS:000600100400028). https://doi.org/10.1021/acs.est.0c05083